



UNIVERSITÄT ZU LÜBECK  
INSTITUTE OF MATHEMATICS AND  
IMAGE COMPUTING

# Automatic Weighting of Non-corresponding Regions in Image Registration

*Automatische Gewichtung von nicht-korrespondierenden Regionen in der Bildregistrierung*

Masterarbeit

im Rahmen des Studiengangs  
Informatik  
der Universität zu Lübeck

vorgelegt von  
David Drobny

ausgegeben und betreut von  
Prof. Dr. Jan Modersitzki  
Institute of Mathematics and Image Computing

mit Unterstützung von  
Dr. Heike Carolus und Dr. Sven Kabus  
Philips Research

Die Arbeit ist im Rahmen einer Tätigkeit bei Philips Research entstanden.

Lübeck, den 28. Januar 2015





## Abstract

This thesis proposes an approach to automatically handle non-corresponding regions in image registration. Non-corresponding regions pose a particular challenge because they cannot be reasonably matched to equivalent regions. Using state-of-the-art algorithms typically leads to unwanted and unrealistic deformations in those image regions. Although there are various approaches considering this topic, they typically focus on specific applications and provide no general solution. The proposed approach is not limited to a single scenario and is thus also designed to handle different distance measures. We present an automatic weight computation, based on the Sum of Squared Differences (SSD) and the Normalized Gradient Field (NGF) distance measure, to reduce the effects of non-corresponding regions in a variational registration framework with an elastic regularizer. While experiments with the NGF distance measure could not show significant differences, several experiments with SSD qualitatively and quantitatively demonstrate the superiority of the proposed approach compared to a standard approach.

## Zusammenfassung

In dieser Arbeit wird ein Ansatz zur automatischen Behandlung von nicht-korrespondierenden Regionen in der Bildregistrierung vorgestellt. Nicht-korrespondierende Regionen stellen eine besondere Herausforderung dar, da sie nicht sinnvoll auf entsprechende Regionen abgebildet werden können. Die Nutzung von Standardverfahren führt typischerweise zu unrealistischen Deformationen in diesen Bildbereichen. Obwohl es verschiedene Ansätze zu dieser Problematik gibt, fokussieren diese typischerweise eine spezifische Anwendung und liefern keine allgemeine Lösung. Der hier vorgeschlagene Ansatz ist nicht auf ein einzelnes Szenario beschränkt und ist daher auch entworfen, verschiedene Distanzmaße handhaben zu können. Wir präsentieren eine automatische Berechnung eines Gewichts, basierend auf dem Sum of Squared Differences (SSD) und dem Normalized Gradient Field (NGF) Distanzmaß, um den Einfluss nicht korrespondierender Regionen innerhalb eines variationellen Registrierungskonzepts mit elastischem Regularisierer zu reduzieren. Während Experimente mit dem NGF Distanzmaß keine signifikanten Unterschiede zeigen konnten, demonstrieren verschiedene Experimente mit SSD sowohl qualitativ als auch quantitativ die Überlegenheit des vorgestellten Ansatzes gegenüber einem Standardverfahren.

---



# Contents

<b>1</b>	<b>Introduction</b>	<b>1</b>
1.1	Medical Image Registration . . . . .	1
1.2	A Challenge in Image Registration: Non-corresponding Regions . .	2
1.3	Approaches meeting this Challenge: State of the Art . . . . .	3
1.4	Contribution of this Thesis . . . . .	5
<b>2</b>	<b>Medical Image Registration</b>	<b>7</b>
2.1	Registration Framework . . . . .	7
2.2	Elastic Regularizer . . . . .	8
2.3	Sum of Squared Differences Distance Measure . . . . .	8
2.4	Normalized Gradient Field Distance Measure . . . . .	8
2.5	Details of the Image Registration Framework . . . . .	10
<b>3</b>	<b>Handling Non-corresponding Regions in Image Registration</b>	<b>13</b>
3.1	Weight Computation for SSD . . . . .	13
3.2	Weight Computation for NGF . . . . .	15
3.3	Weighting of the Distance Measure in Elastic Image Registration .	16
3.4	Parameter Choice . . . . .	18
3.5	Optimization with the Weighted Distance Measure . . . . .	18
<b>4</b>	<b>Experiments and Results</b>	<b>21</b>
4.1	SSD: CT Lung without Tumor . . . . .	22
4.2	SSD: CT Lung with Synthetic Tumor . . . . .	24
4.3	SSD: CT Abdomen . . . . .	27
4.4	NGF: CT Lung with Synthetic Tumor & CT-MRI Abdomen . . .	32
<b>5</b>	<b>Conclusion and Outlook</b>	<b>47</b>
	<b>Bibliography</b>	<b>49</b>
	<b>Appendix A Minimization of the Distance Measure</b>	<b>53</b>

---



# 1 Introduction

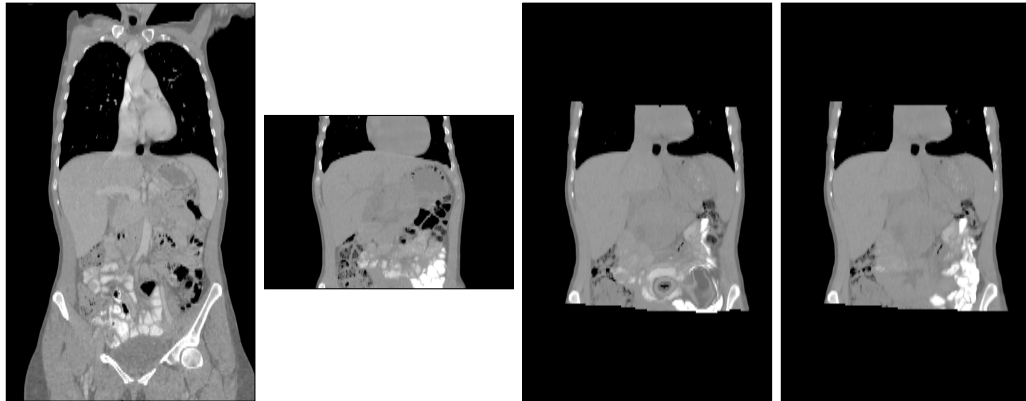
## 1.1 Medical Image Registration

Image registration is a central task in different fields of image processing including medical image processing [1]. Combining the information of two images is often needed in medical applications. Those applications include for example follow-up examinations and image fusion. A direct comparison is not possible because the images are obtained with different settings (e.g. angles, poses, modalities) or the images are of similar (but different) scenes. The task of image registration is to align the images in such a way, that corresponding objects match and information can be compared. Figure 1.1 shows an example of an image registration task. Two computed tomography images are aligned by two different approaches.

Therefor an optimal transformation which describes the spatial relation between the two images has to be determined. The kind of *transformation* as well as the meaning of *optimal* can be chosen and influence the result.

There are several kinds of transformation used in image registration like linear, polynomial, and spline transformation as well as non-parametric transformations which provide a displacement vector for every image position [2]. Optimality is typically evaluated by combining a *distance measure* and a *regularizer* [2]. The distance measure evaluates the similarity of the images and the regularizer evaluates characteristics of the transformation. There are different proposed regularizers, for example the physical motivated elastic and fluid regularizers or the diffusion regularizer [3].

A straight forward approach for the similarity of two images is the difference of the voxel intensities, which leads to the well-known sum of squared differences (SSD) distance measure [1, 2]. Evaluation of the SSD is only reasonable for images with a standardized intensity scale, i.e. a physical phenomenon is always represented by (approximately) the same intensity value. For computed tomography (CT) images the Hounsfield scale provides this characteristic by fixing values for the attenuation of air and water and interpolating other values accordingly [4]. This makes registration with SSD especially suitable and powerful for CT images. Images obtained



**Figure 1.1:** Image registration presented on a abdomen-thorax CT scan and an abdomen CT scan. From left to right: Reference image, template image, template image transformed by a standard elastic registration approach, template image transformed by the proposed approach. Non-corresponding regions, which lead to different transformations, occur as different filling of the intestines in the inferior left part of the abdomen.

by different modalities like magnetic resonance imaging (MRI), positron emission tomography (PET) or single photon emission computed tomography (SPECT) require other distance measures. Different distance measures capable to compare multi-modal images have been proposed, including mutual information [5], normalized cross correlation [6] or normalized gradient fields (NGF) [7].

## 1.2 A Challenge in Image Registration: Non-corresponding Regions

Image registration is typically used to match similar images, as for example two images showing the abdomen of a patient at different points in time. Registration can then be used to match the liver in both images. But there are also situations with fundamental differences besides deformations. For example surgeries, as liver resection, can change the anatomy so that the images of the same patient feature differences. Due to the minimization of the distance measure, these differences are typically compensated by the transformation. In the example of the resection

missing parts of the liver can “grow back” by the registration [8]. This behavior is typically unwanted and can occur in different settings, for example tissue resection [8, 9, 10, 11, 12, 13, 14], tumor growth [9, 13, 14], or display of medical equipment [15, 16]. Further occurrences of non-corresponding regions could also include bone drill out, different filling of digestive organs, or transplantation. In Figure 1.1 the filling of the intestines differs in the reference and the template image. Contrast agent and air moved through the intestines and lead to non-corresponding regions, especially in the left inferior part of the abdomen.

State-of-the-art non-rigid registration algorithms, which do not explicitly handle non-corresponding regions typically estimate a deformation which either shrinks or expands an image region to compensate for the missing correspondence. Effects like this can be seen in the third image of Figure 1.1. Here some areas are expanded and surrounding regions are shrunk to yield a better alignment.

### 1.3 Approaches meeting this Challenge: State of the Art

There are some approaches which cope with the problem of missing correspondences. Most of them are specialized in certain applications, first and foremost in brain resection. Due to the specialization, assumptions can be made to constraint the registration task accordingly.

The task to register images with a medical device displayed in only one image is considered by Berendsen et al. [15, 16]. It is assumed that the segmentation of the medical device is known. Deformation caused by the device can thus be compensated.

Kwon et al. develop a method to register pre- and post-operative brain images [9]. The tumor, resection cavity, and recurrences are segmented based on models which adapt to each scan. They include a-priori knowledge that tumor regions of the pre-operative image will be mapped to resection regions in the post-operative image and recurrences are likely to appear close to resected tumors.

A demon based registration algorithm which accounts for tissue resection was proposed by Nithiananthan et al. [10]. A 4th dimension is added which enables to

remove volumes from the image and map it to a separate image. Here segmentation and registration are computed simultaneously. Non correspondences are only handled for the scenario of tissue to air mapping.

Periaswamy et al. [17] suggests to model the probability for each voxel to be corresponding between both images based on the residual of the images. A local affine registration is used and the parameters are determined with an expectation-maximization approach which iteratively classifies (corresponding/ non-corresponding regions) and registers the images. This approach was tested on different synthetic and real data and is not specialized on a specific application. We adapted the idea of this approach and transfer it to multi-modal image data.

Chitphakdithai et al. [11] propose a registration approach which adapts the idea of [17] to the scenario of brain tumor resection. They use a different registration framework (maximum a posteriori estimation) and also incorporate a-priori knowledge of the kind of non-correspondences, i.e. the area of resected brain tissue is mainly filled with cerebrospinal fluid. An intensity-based prior is used to determine the location of the resection. In further publications this approach was extended to better adapt this specific setting. In [12] an indicator map is described which classifies the kind of correspondence for every image region. Principal component analysis is used to determine the spatial prior for segmentation. To improve results for different time points of tumor treatment more extensions were presented in [13]. Different probability distributions based on the indicator map are introduced to cope with varying intensity values. Also a transformation prior is introduced which allows stronger transformations close to the estimated tumor location. In [14] Markov random fields are used to include spacial knowledge of the resection area into to model.

Beuthien [8] developed a method to match pre- and post-operative liver images when a part of the liver is resected. Therefor the liver vessels are considered. The vessels span through a big part of the liver in a recognizable way and are thus a good aid for the matching. The registration is constrained by length preservation of these vessels.

## 1.4 Contribution of this Thesis

As described in the previous section, most of the state-of-the-art approaches consider missing correspondences for specific applications. This enables a good adaptation to the problem but also further a-priori knowledge has to be included. If it is unclear what kind of non-correspondence occurs in an image pair or if it is unknown whether there are non-corresponding regions at all, a general approach is desirable. Such an approach could be included in a standard registration framework to conveniently register images with or without non-corresponding regions with as little as possible user interaction necessary. Higher accuracy results could probably be achieved by specialized approaches, but in a standard workflow such a general handling of non-correspondences can already be beneficial. Specialized approaches could pose a refinement of the results as a second step when necessary.

We propose an approach which does not include application specific a-priori knowledge and is thus applicable to various scenarios. Following the idea described in [17], we extend an elastic registration framework [2, 18] to reduce the impact of non-corresponding regions by automatically weighting the data term based on the distance measure at every image coordinate.

To demonstrate the feasibility and the advantage compared to a standard approach, we conduct experiments on CT data of the lung, CT data of the abdomen and CT-MR data. We alter the lung images to feature non-corresponding areas. To this end we add an artificial tumor in one image of each pair and show the superior handling of these regions by our proposed approach. The abdomen data naturally feature different kinds of non-corresponding regions and were not altered. Compared to the standard approach, the registration could be improved at different critical regions by the proposed approach. On CT-MR abdomen data it could be shown, that our approach yields neither significant advantages nor disadvantages on multi-modal images.

In this way, we evaluate different scenarios. The general applicability without significant disadvantages of our proposed approach is demonstrated as well as a benefit in handling non-corresponding regions in CT data. Therefore our approach could be suitable to be used in everyday registration applications where non-corresponding regions are possible to occur.



## 2 Medical Image Registration

In this thesis, we extend an existing registration approach. In this chapter focus is put on the starting points of this extension. In 2.1 we give a short introduction into the mathematical framework for image registration. The used regularizer is described in Section 2.2. In Section 2.3 and 2.4 two distance measures are introduced. The unchanged details on the registration algorithm used for our experiments are mentioned in Section 2.5 and further details can be found in the references therein. Details on the extension itself are described in Chapter 3.

### 2.1 Registration Framework

In this first section we give an introduction to the registration framework following [3]. The goal of image registration is to determine an optimal transformation  $\varphi$  which describes the spatial relation between two  $d$ -dimensional images, the reference image  $\mathcal{R}$  and the template image  $\mathcal{T}$ . For most of the clinical applications it holds  $d \in \{2, 3\}$ . The images are continuous mappings with  $\mathcal{R} : \Omega_{\mathcal{R}} \rightarrow \mathbb{R}$  and  $\mathcal{T} : \Omega_{\mathcal{T}} \rightarrow \mathbb{R}$ , where  $\Omega_{\mathcal{R}} \subset \mathbb{R}^d$  and  $\Omega_{\mathcal{T}} \subset \mathbb{R}^d$  are the domains of the images. The continuously differentiable transformation  $\varphi$ ,  $\varphi \in C^1(\Omega_{\mathcal{R}}, \mathbb{R}^d)$  maps every coordinate of the reference domain to a new coordinate and fulfills the Neuman-Zero boundary conditions. The transformation can be split into the identity and the displacement  $u$ ,  $u \in C^1(\Omega_{\mathcal{R}}, \mathbb{R}^d)$ ,

$$\varphi(x) = x + u(x). \quad (2.1)$$

Optimality is achieved in terms of the functional  $\mathcal{J}$ , which combines a distance measure  $\mathcal{D}$  and a regularizer  $\mathcal{S}$  in the following way

$$\mathcal{J}[\mathcal{R}, \mathcal{T}, \varphi] = \mathcal{D}[\mathcal{R}, \mathcal{T} \circ \varphi] + \alpha \mathcal{S}[u] \xrightarrow{\varphi} \min. \quad (2.2)$$

The distance measure  $\mathcal{D}$  provides the driving force of the registrations and minimization of  $\mathcal{D}$  makes the images more similar or less distant respectively, relative to the distance measure. Depending on what kind of distance measure is used to describe the similarity, results can vary. On the other hand the regularizer  $\mathcal{S}$  only

depends on the displacement. This way physically unrealistic or unwanted transformations can be punished with high values. The parameter  $\alpha \in \mathbb{R}^+$  controls the ratio between both terms and can thus regulate the influence of the regularizer.

## 2.2 Elastic Regularizer

Equation (2.2) describes an ill-posed optimization problem, because the solution can be ambiguous (see Hadamard [19] for details on well- and ill-posedness). Therefore it is important to use a regularizer which provides further control of the resulting transformation.

A physical motivated regularizer based on the elastic potential is described here. As presented by Broit [20] the elastic regularizer is defined as

$$\mathcal{S}[u] = \int_{\Omega} \frac{\mu}{4} \sum_{i,j=1}^d (\partial_{x_j} u_i(x) + \partial_{x_i} u_j(x))^2 + \frac{\lambda}{2} (\nabla \cdot u(x))^2 dx, \quad (2.3)$$

with  $\lambda \in \mathbb{R}_0^+$ ,  $\mu \in \mathbb{R}^+$  non-negative scalar parameters accounting for material properties.

## 2.3 Sum of Squared Differences Distance Measure

One of the most straight-forward and intuitive distance measures is the Sum of Squared Differences (SSD) distance measure [1, 2]. The images are compared directly based on the intensity values and integration over the image domain provides a scalar value. A typical formulation of the SSD is

$$\mathcal{D}^{\text{SSD}}[\mathcal{R}, \mathcal{T}] = \frac{1}{2} \cdot \int_{\Omega} (\mathcal{R}(x) - \mathcal{T}(x))^2 dx. \quad (2.4)$$

For future references, we define the residual as

$$r^{\text{SSD}}(x) := \mathcal{R}(x) - \mathcal{T}(x). \quad (2.5)$$

## 2.4 Normalized Gradient Field Distance Measure

If the correspondence of physical quantity and intensity value is not standardized, like it is done by the Hounsfield scale, SSD may not be a suitable distance measure.

As proposed by Haber and Modersitzki [7], Normalized Gradient Field (NGF) is a distance measure which is also applicable for those scenarios. Even if the representations of an object by intensity values do not coincide, they may still be described by the same boundaries. Thus comparing the image gradients is coherent. The gradients are normalized and can be compared either by the inner or the outer product. In this way distinctive gradients can be matched independently of the absolute intensity values and the orientation. We used the formulation of NGF with the inner product:

$$\mathcal{D}^{\text{NGF}}[\mathcal{R}, \mathcal{T}] = \frac{1}{2} \cdot \int_{\Omega} 1 - \left\langle \frac{\nabla \mathcal{R}(x)}{\|\nabla \mathcal{R}(x)\|_{\varepsilon}}, \frac{\nabla \mathcal{T}(x)}{\|\nabla \mathcal{T}(x)\|_{\varepsilon}} \right\rangle^2 dx, \quad (2.6)$$

with

$$\|\nabla I(x)\|_{\varepsilon} := \sqrt{\nabla I(x)^{\top} \nabla I(x) + \varepsilon^2}.$$

This norm regularizes the normalized gradient fields and makes it less sensitive to small values of the image gradients. The parameter  $\varepsilon$  is chosen as suggested by [21]

$$\varepsilon = \frac{\eta}{V} \int_{\Omega} |\nabla I(x)| dx, \quad (2.7)$$

where  $V$  is the volume of the image domain and  $\eta$  estimates the noise level of the image.

With this definition of  $\mathcal{D}^{\text{NGF}}$  the integrand yields values in  $[0, 1]$  at every position  $x$ . Values greater than zero denote gradients with different orientation, where greater differences yield greater values. A value of 0 implies that the image gradients have parallel or anti-parallel orientation. On the one hand a value of 1 denotes gradients which form an angle of  $90^{\circ}$ . On the other hand the integrand also equals 1 if one or both of the gradients equals 0.

The residual of the NGF distance measure is defined as

$$r^{\text{NGF}}(x) := \left\langle \frac{\nabla \mathcal{R}(x)}{\|\nabla \mathcal{R}(x)\|_{\varepsilon}}, \frac{\nabla \mathcal{T}(x)}{\|\nabla \mathcal{T}(x)\|_{\varepsilon}} \right\rangle. \quad (2.8)$$

## 2.5 Details of the Image Registration Framework

In this section, information on the used implementation are given. These methods are not of central concern for this thesis and are thus not described in detail. Further information can be found in the references.

For our experiments we use an implementation based on the approach described in [18] and [22]. As the distance measure  $\mathcal{D}$ , we used either SSD or NGF while a regularizer  $\mathcal{S}$  based on the elastic potential is used (see Sections 2.2-2.4 for details). In general, the optimize-then-discretize strategy is followed. This means firstly the calculus of the optimization problem is done analytically and secondly results are transferred to a discrete formulation to solve it numerically.

The cell-centered discretization  $\Omega_h$  of  $\Omega$  into  $n_j$  grid points in the dimensions  $j \in \{1, \dots, d\}$  can be described as follows:

$$\Omega_h := \{x_{i_1, \dots, i_d} = ((i_j - 0.5)h_j)_{j=1, \dots, d} \mid i_j = 1, \dots, n_j\}, \quad (2.9)$$

with the grid spacing  $h_j = n_j^{-1}$ . The pair of a coordinate  $x \in \mathbb{R}^d$  and a value  $w \in \mathbb{R}^u$  is called pixel (picture element) for  $d = 2$  and voxel (volume element) for  $d > 2$ . Typical values for  $u$  are 1 (intensities, grayscale images) and 3 for color images. In (2.9) coordinates are normalized to the interval of  $[0, 1]$  in each dimension. For arbitrary coordinates in  $[a_j, b_j]$  the spacing is scaled with the length of the interval to  $h_j = \frac{b_j - a_j}{n_j}$  and  $a_j$  has to be added as an offset to each coordinate. For further details see [2]. With a suitable interpretation of the grid spacing, coordinates can be transferred to measured values for distances in the real world with the origin as an arbitrary reference point. Given the interpretation of the spacing we can this way for example transform the information of a tumor having a maximal diameter of 30 voxel to a real world length of 20 mm. Therefore we can also associate a size with each voxel, i.e. the grid spacing in a given unit.

Partial derivatives which occur during the optimization are discretized by central difference quotients [2]. The numerical optimization is then performed by a conjugate gradients (CG) solver [23].

The elastic registration is initialized by an affine registration [2]. This enables a pre-alignment which avoids local minima of the elastic registration. This has shown to be especially important if one image only depicts a part of the anatomy of the other one. In this situation the smaller volume can be shifted significantly within the other one, which may lead the elastic registration to get stuck in local minima when no pre-alignment is used.

The affine pre-registration as well as the elastic registration both make use of a multi-level approach [24]. Therefor the discretized images are downsampled to certain resolutions. Registration starts on a coarse level and iteratively propagates the computed displacement to the next finer level. This technique can speed up convergence and also make it more robust. On coarse levels only coarse structures are aligned and thus local minima are avoided.



## 3 Handling Non-corresponding Regions in Image Registration

In this chapter a strategy to handle non-corresponding regions is explained. First in Section 3.1 an automatic weight for the SSD distance measure is presented. Then in Section 3.2 we show how the weight can be adapted to cope with NGF as the distance measure. In Section 3.3 the combination of the weight into the distance measure is shown. Section 3.4 describes how the parameters of the approach have been determined. Finally in Section 3.5 derivatives needed for the numerical solution are presented.

### 3.1 Weight Computation for SSD

As shown in 1.2, applying image registration to real data often brings up the problem of missing correspondences. This means an object or a part of it which is shown in one image is not represented in the other one. Those regions can lead to unwanted or unrealistic registration results.

In Section 1.3 different approaches were described which all but one handle non-corresponding regions for specific applications. Contrary to that, our proposed automatic weighting aims for the mutuality of different non-correspondences so we can deal with them in a general way.

The weighting, we apply, automatically adapts to the images and decreases the influence of non-corresponding regions. Therefor a local measure for the degree of correspondence has to be estimated. This is done with an approach which is based upon conditional probabilities [25]. In this section we seize the central idea presented by Periaswamy and Farid [17] for the SSD distance measure. However, we introduce new terms and complete missing information here.

To evaluate the degree of correspondence we compare two assumptions. The first assumption,  $A_1$ , assumes that there is a relationship of the voxels of  $\mathcal{R}$  and  $\mathcal{T}$  which is explained by the transformation vector field  $\varphi = \text{id} + u$ .

### 3.1 Weight Computation for SSD

---

The second assumption,  $A_2$ , states a non-correspondence of the voxels.

Under  $A_1$  a Gaussian distribution with zero mean for the residual  $r^{\text{SSD}}$  is assumed. This reflects the fact, that for similar images the residual is expected to be low in bigger parts of the image and high values are less probable. The probability of a certain intensity value of the residual at a position  $x$  is thus given by

$$Pr(r^{\text{SSD}}(x) | A_1) = \frac{1}{\sigma\sqrt{2\pi}} e^{-\frac{r^{\text{SSD}}(x)^2}{v \cdot \sigma^2}}, \quad (3.1)$$

where  $\sigma^2 = \text{var}(r^{\text{SSD}}(x))$  is the variance of the residual image and  $v$  is a positive parameter which can be used to handle characteristics of the image pair.

In the following we will drop the scaling of the Gaussian distribution in correspondence to the reference publication [17] and define the weight  $W_1^{\text{SSD}}(x)$ ,  $W_1^{\text{SSD}} : \mathbb{R}^d \rightarrow [0, 1]$ ,

$$W_1^{\text{SSD}}(x) := e^{-\frac{r^{\text{SSD}}(x)^2}{v \cdot \sigma^2}} \quad (3.2)$$

to describe this unscaled version of the distribution.  $W_1^{\text{SSD}}$  maps to values between 0 and 1. The lower bound is given by the characteristics of the Euler function. The numerator of the fraction in the exponent is non-negative due to the quadrature and the factors of the denominator are non-negative by definition. The lower limit of the fraction in the exponent is therefore 0, The upper limit of the whole exponent is 0 and  $W_1^{\text{SSD}}$  thus has an upper limit of 1.

The residual is assumed to have a uniform distribution under  $A_2$ . Since we do not have prior knowledge about the type of non-correspondence, any value of the residual has the same probability to depict a non-correspondence. We define a weight for all residual values under the second assumption as  $W_2^{\text{SSD}}$  which, in analogy to  $W_1^{\text{SSD}}$ , equals an unscaled uniform probability distribution.

$$W_2^{\text{SSD}}(x) := p \quad (3.3)$$

is therefore constant with  $p \in [0, 1]$ .

The amount of regions without correspondence can vary highly, thus it is infeasible to predict the a-priori probabilities for  $A_1$  and  $A_2$  without further knowledge of the image data. Because of this we assume that the a-priori probabilities for both assumptions are equal. In accordance with the Bayes theorem [26] we obtain

the weight  $W_*^{\text{SSD}}(x)$ ,  $W_*^{\text{SSD}} : \mathbb{R}^d \rightarrow [0, 1]$  which, given the residual, indicates the probability<sup>1</sup> for every voxel to have a valid correspondence:

$$W_*^{\text{SSD}}(x) = \frac{W_1^{\text{SSD}}(x)}{W_1^{\text{SSD}}(x) + W_2^{\text{SSD}}(x)} = \frac{W_1^{\text{SSD}}(x)}{W_1^{\text{SSD}}(x) + p}. \quad (3.4)$$

Given the lower bound of 1 for  $W_1^{\text{SSD}}$ , the lower bound for  $W_*^{\text{SSD}}$  follows directly. The upper bound of 1 is reached for maximal  $W_1^{\text{SSD}}$  (1) and minimal  $p$  (0) and hence is 1 as well.

### 3.2 Weight Computation for NGF

In 2.4 it was explained that SSD is limited to the registration of CT images. In order to make the weighting approach applicable to multi-modal images, we adapt it for the normalized gradient field distance measure.

If a distance measures provides residuals with certain characteristics (as the SSD does), they can be substituted for  $r^{\text{SSD}}$  in (3.2) without further need of adaption. The following assumptions are required:

- (a) The residual  $r$  is normally distributed with a mean of 0 and
- (b) residual values of 0 contribute to a small distance measure.

Note, that the absolute values of  $r$  are irrelevant due to the normalization by the variance.

When defining the residual for NGF as in (2.8) the criterion (b) is not fulfilled since values of 0 lead to the maximal value in  $\mathcal{D}^{\text{NGF}}$ . The interpretation of the residual values is thus negated. If the whole integrand of  $\mathcal{D}^{\text{NGF}}$  was used as the residual instead, the criterion (b) is fulfilled on the one hand. On the other hand quadrature eliminates negative values, so this term cannot have a symmetrical distribution with zero mean and thus does not meet the requirement (a).

To use NGF with the with our weighted approach,  $W_1^{\text{NGF}}(x)$ ,  $W_1^{\text{NGF}} : \mathbb{R}^d \rightarrow [0, 1]$  is computed as

$$W_1^{\text{NGF}} := 1 - e^{-\frac{r^{\text{NGF}}(x)^2}{v \cdot \sigma^2}}. \quad (3.5)$$

---

<sup>1</sup>Probability is not used in the mathematical but in a more colloquial way at this point.

In this way the probabilities are inverted to account for the inverted nature of this residual. Low values of  $r^{\text{NGF}}$  indicate minimal similarity and yield a minimal value of  $W_1^{\text{NGF}}$ .

Computation of  $W_*^{\text{NGF}}(x)$ ,  $W_*^{\text{NGF}} : \mathbb{R}^d \rightarrow [0, 1]$  is done without further changes in analogy to (3.4):

$$W_*^{\text{NGF}}(x) = \frac{W_1^{\text{NGF}}(x)}{W_1^{\text{NGF}}(x) + p}. \quad (3.6)$$

The argumentation for upper and lower bounds for  $W_1^{\text{NGF}}$  and  $W_*^{\text{NGF}}$  is analogously to the SSD case.

### 3.3 Weighting of the Distance Measure in Elastic Image Registration

In the following we will write  $W$  and  $W_*$  as a short form if a statement holds for the respective formulation of both distance measures as well as  $\mathcal{D}$  and  $\mathcal{D}_{W_*}$  in analogy.

The weight  $W_*^{\text{SSD}}$  is included in the SSD distance measure  $\mathcal{D}^{\text{SSD}}$  to multiplicatively weight the residual:

$$\mathcal{D}_{W_*}^{\text{SSD}}[\mathcal{R}, \mathcal{T}(\varphi)] = \frac{1}{2} \cdot \int_{\Omega} [W_*^{\text{SSD}}(x) \cdot (\mathcal{R}(x) - \mathcal{T}(\varphi(x)))]^2 dx. \quad (3.7)$$

Analogously the weight  $W_*^{\text{NGF}}$  is included in the NGF distance measure:

$$\mathcal{D}_{W_*}^{\text{NGF}}[\mathcal{R}, \mathcal{T}(\varphi)] = \frac{1}{2} \cdot \int_{\Omega} 1 - \left[ W_*^{\text{NGF}}(x) \cdot \left\langle \frac{\nabla \mathcal{R}(x)}{\|\nabla \mathcal{R}(x)\|_{\varepsilon}}, \frac{\nabla \mathcal{T}(\varphi(x))}{\|\nabla \mathcal{T}(\varphi(x))\|_{\varepsilon}} \right\rangle \right]^2 dx. \quad (3.8)$$

$W_*$  is in the range of  $[0, 1]$ . This implies that the voxel wise distance measure is unchanged only if  $W_*(x) \equiv 1$  and down weighted else. Thus the inequality

$$\mathcal{D}_{W_*}[\mathcal{R}(x), \mathcal{T}(\varphi(x))] \leq \mathcal{D}[\mathcal{R}(x), \mathcal{T}(\varphi(x))] \quad (3.9)$$

holds. If the distance measure changes and the regularizer stays the same, the balance of those terms and thus the elasticity changes. A decrease in the data

term means a bigger influence of the regularizer, the deformation becomes less elastic.

Since we rely on a well tested standard value of  $\alpha$  to control the elasticity, we want to keep the ratio of distance measure and regularizer unchanged. Therefore we have to compensate for the reduced weight of the distance measure caused by the weighting with  $W_*$ .

This could be achieved by linear scaling of  $W_*$  with the factor  $s$ , where

$$s = \sqrt{\frac{\mathcal{D}[\mathcal{R}, \mathcal{T}(\varphi)]}{\mathcal{D}_{W_*}[\mathcal{R}, \mathcal{T}(\varphi)]}} \quad (3.10)$$

and

$$W := s \cdot W_*. \quad (3.11)$$

Due to the complex nature of  $s$ , this factor may change the convexity of the optimization task. Also the computational complexity in each iteration would increase significantly. On the other hand, experiments have shown, that the change of  $s$  in each iteration is very small. Based on these reasons, we decided to approximate  $s$  once at the beginning of the optimization and then keep it constant on each level  $l$  of the multi-level approach. Therefore (3.10) is computed for  $\varphi = \varphi_l^0$ , where  $\varphi_l^0$  denotes the initial deformation on level  $l$ .

The scaled probability map  $W$  is not limited to the range of  $[0, 1]$  but can have values larger than one. Thus the influence of some regions on the data term is reduced while the influence of rest is enhanced.

The final formulation of the weighted distance measure results from substituting  $W_*$  in (3.7) and (3.8) by the scaled weight  $W$ . For the SSD distance measure it leads to

$$\mathcal{D}_W^{\text{SSD}}[\mathcal{R}, \mathcal{T}(\varphi)] = \frac{1}{2} \cdot \int_{\Omega} [W^{\text{SSD}}(x) \cdot (\mathcal{R}(x) - \mathcal{T}(\varphi(x)))^2] dx, \quad (3.12)$$

and for NGF accordingly

$$\mathcal{D}_W^{\text{NGF}}[\mathcal{R}, \mathcal{T}(\varphi)] = \frac{1}{2} \cdot \int_{\Omega} 1 - \left[ W^{\text{NGF}}(x) \cdot \left\langle \frac{\nabla \mathcal{R}(x)}{\|\nabla \mathcal{R}(x)\|_{\varepsilon}}, \frac{\nabla \mathcal{T}(\varphi(x))}{\|\nabla \mathcal{T}(\varphi(x))\|_{\varepsilon}} \right\rangle \right]^2 dx. \quad (3.13)$$

With this extended data term and the unaltered elastic regularizer  $S[u]$ , registration is performed according to the implementation described in 2.5. With the scaled Weight  $W$  on the one hand and an unchanged regularizer on the other hand, we ensure a similar transformations for corresponding regions independent of using the the original implementation with  $\mathcal{D}$  or the proposed approach with  $\mathcal{D}_W$ . Differences in the handling of non-corresponding regions can thus be explained by effects of the proposed approach and not by substantial differences of the elasticity.

### 3.4 Parameter Choice

In the previous section two parameters,  $v$  and  $p$ , have been introduced to adapt the weight computation to different settings. These parameters are desirable to adjust the effect of the weight for specific needs. Furthermore they are essential to cope with the fundamental disparity of different distance measures. While the scaling of the weight to retain the ratio of distance measure and regularizer could be automated, useful parameters for  $v$  and  $p$  have been determined empirically. An automated computation is thinkable but is beyond the scope of this work. The parameters used in the experiments described in the next chapter are summarized in Table 3.1.

### 3.5 Optimization with the Weighted Distance Measure

In Section 2.1 the mathematical framework of the registration task was described. Essentially, the registration accords to the minimization of the functional  $\mathcal{J}$  as described in (2.2).  $\mathcal{J}$  is a sum of the distance measure  $\mathcal{D}$  and the regularizer  $\mathcal{S}$ . Because both summands are integrals and thus non-negative, optimization of  $\mathcal{J}$

**Table 3.1:** Exemplary values for both parameters of the proposed approach for the different test data sets.

	$p$	$v$
CT lung	0.0025	16
CT abdomen	0.0025	8
CT-MR	0.01	4

can be split up in the optimization of  $\mathcal{D}$  and  $\mathcal{S}$ .

Calculation of the Gâteaux differential of  $\mathcal{S}$  as described in [27] leads to the Euler-Lagrange Equation

$$-\mu\Delta u(x) - (\lambda + \mu)\nabla \cdot \nabla u(x) = 0, \quad x \in \Omega. \quad (3.14)$$

As the regularizer is unchanged in the proposed approach, this calculation is not described further.

In the following we present the results for the minimization of the distance measure  $\mathcal{D}$ . The calculations can be found in detail in the appendix A.

Let  $F$  denote the integrand of the distance measure

$$F^{\text{SSD}}(x) := [W^{\text{SSD}}(x) \cdot r^{\text{SSD}}(x)]^2 \quad (3.15)$$

and

$$F^{\text{NGF}}(x) := 1 - [W^{\text{NGF}}(x) \cdot r^{\text{NGF}}(x)]^2. \quad (3.16)$$

Then an optimum of  $F$  is given by

$$\nabla_{\varphi} F(x) = 0, \quad x \in \Omega, \quad (3.17)$$

where  $\nabla_{\varphi}$  denotes the gradient operator with respect to the transformation  $\varphi$ . In the results this operator vanishes and only the gradient with respect to the coordinates remains. In the following  $(\nabla \cdot)_i$  denotes the  $i$ -th component of a derivative.

First the derivative for the SSD distance measure is presented component wise:

$$(\nabla_{\varphi} F^{\text{SSD}})_i = 2 (W \cdot r^{\text{SSD}}) \cdot [(\nabla_{\varphi} W)_i \cdot r^{\text{SSD}} - W \cdot (\nabla \mathcal{T}_{\varphi})_i]. \quad (3.18)$$

The derivative of the weight  $W$  holds for both distance measures

$$(\nabla_{\varphi} W)_i = s \cdot \frac{p (\nabla_{\varphi} W_1)_i}{(W_1 + p)^2}, \quad (3.19)$$

while  $W_1$  depends on the distance measure. For SSD it yields

$$(\nabla_{\varphi} W_1^{\text{SSD}})_i = W_1^{\text{SSD}} \cdot \frac{(r^{\text{SSD}})^2 \cdot \nabla_{\varphi} \sigma^2 - 2\sigma^2 \cdot r^{\text{SSD}} \cdot (\nabla \mathcal{T}_{\varphi})_i}{v \cdot (\sigma^2)^2}. \quad (3.20)$$

The derivative of the standard deviation for discrete images is given by

$$\nabla_{\varphi}\sigma^2 = -\frac{2}{n} \sum_{k=1}^n \left( (r^{\text{SSD}}(x_k)) - \text{mean}(r^{\text{SSD}}) \right) \cdot \left( (\nabla\mathcal{T}_{\varphi})_i(x_k) - \text{mean}(\nabla\mathcal{T}_{\varphi}) \right), \quad (3.21)$$

where  $n$  is the number of voxels.

The NGF distance measure yields a derivative similar to 3.18:

$$(\nabla_{\varphi}F^{\text{NGF}})_i = -2(W \cdot r^{\text{NGF}}) \cdot [(\nabla_{\varphi}W)_i \cdot r^{\text{NGF}} + W \cdot (\nabla_{\varphi}r^{\text{NGF}})_i], \quad (3.22)$$

with  $\nabla_{\varphi}W$  as in (3.19) and

$$(\nabla_{\varphi}r^{\text{NGF}})_i = \sum_{k=1}^d \frac{\nabla((\nabla\mathcal{T}_{\varphi})_k)_i}{\|\nabla\mathcal{T}_{\varphi}\|_{\varepsilon}} \cdot \left( \frac{(\nabla\mathcal{R})_k}{\|\nabla\mathcal{R}\|_{\varepsilon}} - r^{\text{NGF}} \cdot \frac{(\nabla\mathcal{T}_{\varphi})_k}{\|\nabla\mathcal{T}_{\varphi}\|_{\varepsilon}} \right). \quad (3.23)$$

The derivative of  $W_1^{\text{NGF}}$  is similar to the SSD case but with opposite sign:

$$(\nabla_{\varphi}W_1^{\text{NGF}})_i = -W_1^{\text{NGF}} \cdot \frac{(r^{\text{NGF}})^2 \cdot \nabla_{\varphi}\sigma^2 - 2\sigma^2 \cdot r^{\text{SSD}} \cdot (\nabla\mathcal{T}_{\varphi})_i}{v \cdot (\sigma^2)^2}. \quad (3.24)$$

The equations (3.14) and (3.17) can be solved numerically with respect to certain boundary conditions. For details on the specific numerical methods see [22].

## 4 Experiments and Results

This chapter describes the experiments conducted including the used data and evaluation of the results.

In each experiment medical image pairs of different databases are registered with both approaches, the standard and the extended approach, and the same settings. Each experiment is described and evaluated in a separate section. The first three experiments make use of the SSD distance measure, the last one uses NGF.

In the first Section 4.1 we apply both approaches on inhale-exhale lung CT images to show their similar results on an established scenario. The second experiment, described in Section 4.2, uses the same CT lung images but with artificially added tumors as non-corresponding regions. Here we compare the differences in the results of both approaches in areas where non-correspondences appear. Our extended approach proves to be superior in this experiment, supported with quantitative evaluations of the tumor volume change. Real life CT data of the abdomen without any alterations support the results obtained on the lung data. These experiments with more complex image data are described in Section 4.3. To evaluate results with the NGF distance measure and to compare it with the SSD results, the altered CT lung images of the second experiment are evaluated with NGF. Additionally multi-modal data in the form of CT-MR cases of the abdomen are evaluated as well. Section 4.4 describes the results of these experiments which could not show significant differences between the two approaches for the NGF distance measure.

Note that in this chapter all images are discrete.

In this chapter several figures show examples of the registration results of both approaches. For each example two figures, each consisting of six images, is presented. These figures are always structured the same way. To avoid repetitive captions the configurations of both types of figure are described here in a general way. The captions of the individual figures first refer to the type of figure and then only give information for the specific example.

**Configuration (a), left page** These figures give an overview about the images which are registered and the respective results of the two approaches. The reference  $\mathcal{R}$ , the template  $\mathcal{T}$  and the difference image of reference and template  $\mathcal{R} - \mathcal{T}$  demonstrate the initial registration task. The transformed templates of the standard algorithm  $\mathcal{T}(\varphi_{\text{std}})$  and the extended algorithm  $\mathcal{T}(\varphi_{\text{ext}})$  as well as the difference of the warped templates  $\mathcal{T}(\varphi_{\text{ext}}) - \mathcal{T}(\varphi_{\text{std}})$  show the results of the registration.

**Configuration (b), right page** This type of figure gives further details about the registration results. The residual images of the standard algorithm  $\mathcal{R} - \mathcal{T}(\varphi_{\text{std}})$  and the extended algorithm  $\mathcal{R} - \mathcal{T}(\varphi_{\text{ext}})$  show how well the images got aligned by the registration. An enlarged detail of the difference image of the warped template images  $\mathcal{T}(\varphi_{\text{ext}}) - \mathcal{T}(\varphi_{\text{std}})$  focuses on specific regions of interest. The volume change resulting from the standard algorithm  $\det(\nabla(\varphi_{\text{std}}))$  and the extended algorithm  $\det(\nabla(\varphi_{\text{ext}}))$  give an impression of how the transformation looks like. Orange and red colors in the volume change denote shrinkage, while blue values denote expansion. Finally the weight  $W$  of the extended algorithm gives information about on which regions the data term was down-weighted. Values close to 0 in  $W$  are shown dark and values close to the maximum are shown white.

## 4.1 SSD: CT Lung without Tumor

The first experiments aims to show that standard and extended approach yield similar results for data without relevant non-correspondences. We chose lung data with a pair of inhale-exhale images, because deformation stems from the breathing motion and is thus relative predictable. This helps to avoid unclear influences on the transformation and makes the results easier to explain. We use five inhale-exhale lung 3D-CT image pairs provided by the DIR-lab project [28]. Each image has a size of  $256 \times 256$  voxel in-slice, depicting the thorax with a voxel size between  $(0.97 \times 0.97)$  and  $(1.16 \times 1.16)$  mm<sup>2</sup> and a slice thickness of 2.5 mm. For each image pair 300 corresponding reference landmarks are provided enabling quantitative analysis of the registration results.

**Table 4.1:** TRE in mm of all unaltered lung images (cases 1-5) and the overall mean, showing slightly better result for registration with the standard approach. The evaluation is based on 300 landmark pairs. Case 5 is shown in Figure 4.1 as an example.

	case 1	case 2	case 3	case 4	case 5	$\sum$
no registration	3.89	4.34	6.94	9.83	7.48	6.50
standard approach	1.03	1.09	1.59	1.68	1.77	1.43
extended approach	1.04	1.12	1.67	1.68	1.80	1.46

Evaluation of the original CT lung data sets shows basically no significant difference between the results of the standard and the extended algorithm. In Figure 4.1 and 4.2 the results of case 5 are shown as an example. Especially the difference image of the transformed template images  $\mathcal{T}(\varphi_{ext}) - \mathcal{T}(\varphi_{std})$  makes the little difference clear.

To quantitatively compare registration results given landmarks which are either manual, semi-automatic or even full-automatic can be evaluated. A set of landmarks identifies recognizable (anatomical) points in both discrete images  $R$ ,  $T$ . This way the correspondence between the representations of a physical point in both images,  $x_R$  and  $x_T$  is given. These landmarks can be used to evaluate the accuracy of a transformed template image  $T(\varphi)$  [29]. Therefore the Euclidean distance between the mapped landmark position  $x_R^{pred} := \varphi(x_T)$  (the prediction) and the actual position  $x_R^{actual}$  is evaluated

$$\text{TRE}(x_T) := \left\| x_R^{pred} - x_R^{actual} \right\|_2. \quad (4.1)$$

This is called the Target Registration Error (TRE) for one landmark pair. For a set of landmarks interesting features may be average TRE, maximal TRE, quantiles or standard deviation of the TRE.

The average TRE of all cases of the lung database as well as the overall average is listed in Table 4.1. In general the standard approach yields slightly better (lower) TRE values on these data. Although the average difference can be considered very small with only 0.03 mm (note that misalignment of a landmark by one voxel in

slice already results in a TRE between 0.97 mm and 1.16 mm and a misalignment of one slice results in a TRE of 2.5 mm).

## 4.2 SSD: CT Lung with Synthetic Tumor

An example where non-corresponding regions become evident is two pictures taken at different points in time documenting tumor growth. To simulate such images, we altered each of the template lung images by adding an ellipsoid into the right lung, once centered and once peripheral. Besides this change, the experiment is conducted like the previous one. The synthetic nature of the tumor as well as the given landmarks enable quantitative analysis of the registration results.

Because this experiment only differs from the previous one in Section 4.1 in the synthetic tumor in the template image, the results are very similar. This local change leads to local differences in the registration. In the biggest area the transformed template images of both experiments are basically the same. Only in the area around the tumor location distinctive differences can be seen. The standard approach clearly compresses the tumor for every case. By reducing the volume, the distance measure is decreased as well. On the other hand, the extended approach only slightly changes the tumor volume.

Figure 4.3 and 4.5 illustrate two examples with peripheral tumors. In both cases the tumor is compressed significantly by the standard algorithm (see the deformed template images  $\mathcal{T}(\varphi_{std})$ ) while the extended algorithm yields a transformed template  $\mathcal{T}(\varphi_{ext})$  with only marginal tumor shrinkage. Although the tumor located at the diaphragm (Figure 4.3  $\mathcal{T}$ ) is moved in inferior direction along with the breathing motion, its shape is retained by the extended approach. The differences in the remaining lung are small as can be seen in the difference images  $\mathcal{T}(\varphi_{ext}) - \mathcal{T}(\varphi_{std})$ . The Weight  $W$  (Figure 4.4 and 4.6), computed in the end of the registration, mainly shows the region of the tumor as a dark blob which indicates a low weight and thus a assumed non-correspondence. Because of the low weight in the distance measure the transformation of these regions is dominated by the regularizer and thus strong deformation of the tumor is avoided. This also becomes apparent when looking at the determinant of the Jacobian of the transformation  $det(\nabla(\varphi_{std}))$ ,

**Table 4.2:** TRE in mm of all lung images with synthetic tumor (cases 1-5) and the overall mean. Tumor presence slightly impairs the TRE for the standard approach and improves the TRE of the extended approach. The evaluation is based on 300 landmark pairs. Cases 2 and 3 are shown as examples in Figures 4.3-4.6.

tumor	approach	case 1	case 2	case 3	case 4	case 5	$\sum$
peripheral	standard	1.04	1.09	1.59	1.70	1.79	1.44
	extended	1.05	1.10	1.62	1.68	1.77	1.44
central	standard	1.03	1.11	1.63	1.73	1.79	1.46
	extended	1.04	1.10	1.64	1.72	1.78	1.45

indicating the volume change. The standard approach yields a very strong volume change in the area of the tumor while the rest of the image is very homogeneous. Our proposed approach deforms the tumor area with only a marginal difference to the surrounding area.

When considering the average TRE for the altered lung images, the advantage of the standard approach disappears. The average TRE of the standard approach is 1.44 mm for peripheral tumors and 1.46 mm for central tumors. The extended approach yields very similar results of 1.44 mm and 1.45 mm. This means that, compared to the previous experiment without tumors, the error of standard approach increases while the error of the extended approach decreases. The error increase is expected. The transformation changes locally due to the tumor while the landmarks in this area stay unchanged. The error decrease of the extended approach on the other hand is somehow contra intuitive. When looking at the average TRE of the unaltered images (Table 4.1) we find the biggest difference between both approaches for case 3. For this case the TRE of the extended approach is 0.08 mm higher. The difference for this case with included tumor is reduced to 0.03 mm for the peripheral tumor and only 0.01 mm for the central tumor. This suggests, that the disadvantage of the extended approach for the unaltered lung images is balanced by the the presence of the tumor. It can be assumed that worse average TRE values of the extended approach compared to the standard approach are due to falsely detected non-correspondences. These small areas with a low weight negatively influence the transformation. If there is a real non-corresponding region, as introduced by the synthetic tumor, this region

**Table 4.3:** Volume change of the tumor in the altered lung images relative to the baseline deformation, showing the different effect of the standard and the extended algorithm. For both algorithms, the relative volume change of each test image pair with central and peripheral tumor as well as the overall mean value is given. Cases 2 and 3 are shown as examples in Figures 4.3-4.6.

tumor	approach	case 1	case 2	case 3	case 4	case 5	$\Sigma$
peripheral	standard	-50%	-52%	-37%	-30%	-45%	-43%
	extended	-14%	-8%	-6%	-11%	-11%	-10%
central	standard	-71%	-72%	-61%	-56%	-70%	-66%
	extended	-14%	-13%	-10%	-15%	-14%	-13%

yields a low weight and the false positive regions might not appear anymore. In this way, the overall TRE may be improved because less false positive low weights occur.

Although the advantage of the extended approach is clearly visible in the example images, TRE evaluation shows no significant difference. This can be explained by the limited number of landmarks. The 300 landmarks do not cover the lung entirely, so that especially the peripheral tumors barely have landmarks close enough to influence their transformation. The central tumors are more likely to have landmarks close by, but still this number of landmarks is very little to have a strong influence on the average TRE.

To evaluate the difference of the transformations at the tumor region quantitatively, we analyze the volume change of the tumor. The ground-truth volume is computed with the baseline deformation, i.e. the deformation resulting from standard registration of the unaltered images. This is done to estimate the volume of the tumor region, only deformed by the breathing motion. If the registration of the altered images was not influenced by the tumor, we assume the deformation to be the same as the baseline deformation. Thus we compare the volume resulting from the registration of the altered images with the ground-truth volume. The relative volume change for central and for peripheral tumors is shown in Table 4.3. The standard algorithm yields an average reduction of the tumor volume of 66% for central location and 43% for peripheral location while the extended algorithm

better retains the size of the tumor with an average reduction of 19% and 14%, respectively. The magnitude of the volume change depends on the tumor location. The peripheral tumors are located on the lung boundary. Since the surrounding tissue of the lung has intensity values similar to the tumor, the volume of the tumor part located outside of the lung is less deformed. This results in less volume change for the peripheral tumors.

### 4.3 SSD: CT Abdomen

Registration of abdomen images is typically more complex than of lung images since more effects can contribute to the deformation. Differences in the pose of the patient as well as differences in the filling of digestive organs or breathing can deform the anatomy significantly.

The abdomen CT cases we investigated pose different challenges. The main difficulty is posed by contrast agent and gas inside the digestive organs at varying locations. Besides this also tumor growth and resection yield non corresponding regions. In total we evaluated the results of nine image pairs. The images have a size of  $512 \times 512$  voxel in-slice and covering the abdomen with a voxel size between  $(0.69 \times 0.69)$  and  $(1.17 \times 1.17)$  mm<sup>2</sup> and slice thickness between 0.45 and 5 mm.

The experiments conducted on these CT abdomen images support the results of the previous experiments. Using the standard approach several regions show unwanted transformations due to non-correspondences which can be avoided with our proposed approach. In the following three representative examples are described.

The first example (Figure 4.7 and 4.8) shows strong differences in the filling of the small intestine. Especially in the reference image, a big part of the intestine in the right body part is filled with gas. In the template image there are less and different parts of the intestine filled with gas. During the registration of the standard approach, the big differences in gas-tissue overlap are reduced by either shrinking or dilatation of gas areas. Comparing the inferior right part of the intestine of the deformed template of both approaches,  $\mathcal{T}(\varphi_{std})$  and  $\mathcal{T}(\varphi_{ext})$ , it can be seen, that the volume filled with gas is reduced in the standard approach. This is due to the lack of correspondence in the reference image. The extended approach avoids

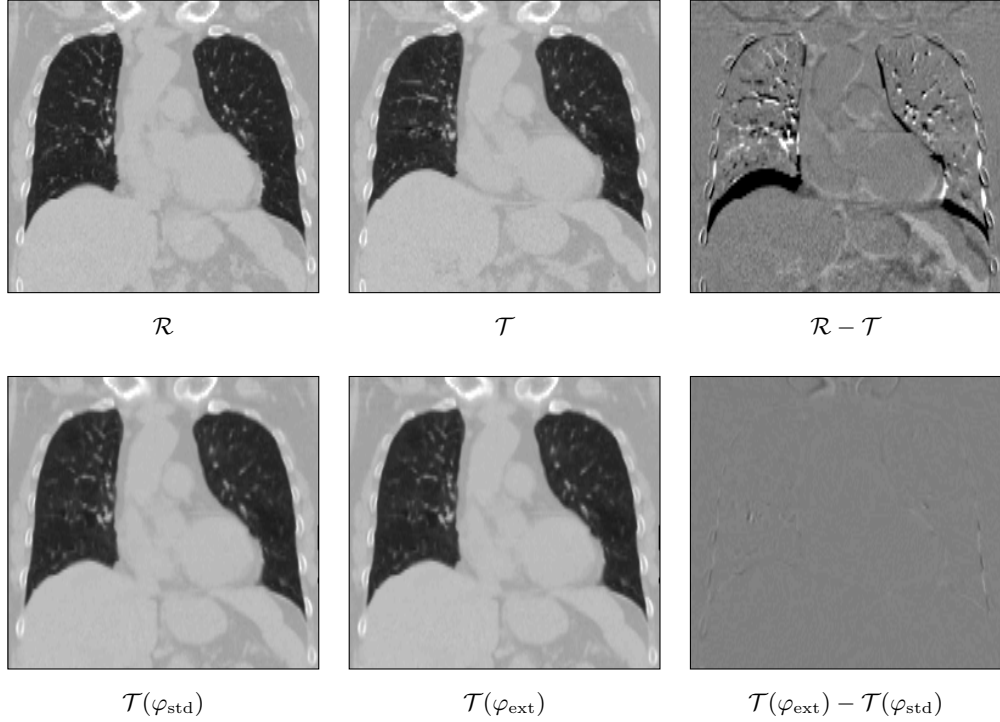


**Figure 4.1: (a)** Coronal view of the 3D results (using  $\mathcal{D}_W^{SSD}$ ) for case 5 of the CT lung database. The unaltered lung images yield almost identical results for both approaches. The average TRE of this case can be found in Table 4.1.

this reduction, because the distance measure has a low weight in this image region as can be seen in the weight  $W$ . Other areas of the template image are dilated by the standard approach so that bigger volumes with low intensity matching the intestinal gas appear. The Jacobians of the transformations,  $\det(\nabla(\varphi_{std}))$  and  $\det(\nabla(\varphi_{ext}))$ , also indicate that strong deformation is located at the intestines of the right body. Comparing the Jacobians, it can be seen that the standard approach yields stronger deformation in the discussed region of the intestines.

In the second example (Figure 4.9 - 4.10) a noticeable bad registration result of the standard approach is shown. The intestines are partly filled with contrast agent, smaller parts are also filled with gas. The locations of the contrast agent differ between reference image  $\mathcal{R}$  and template image  $\mathcal{T}$  as well as the intensity

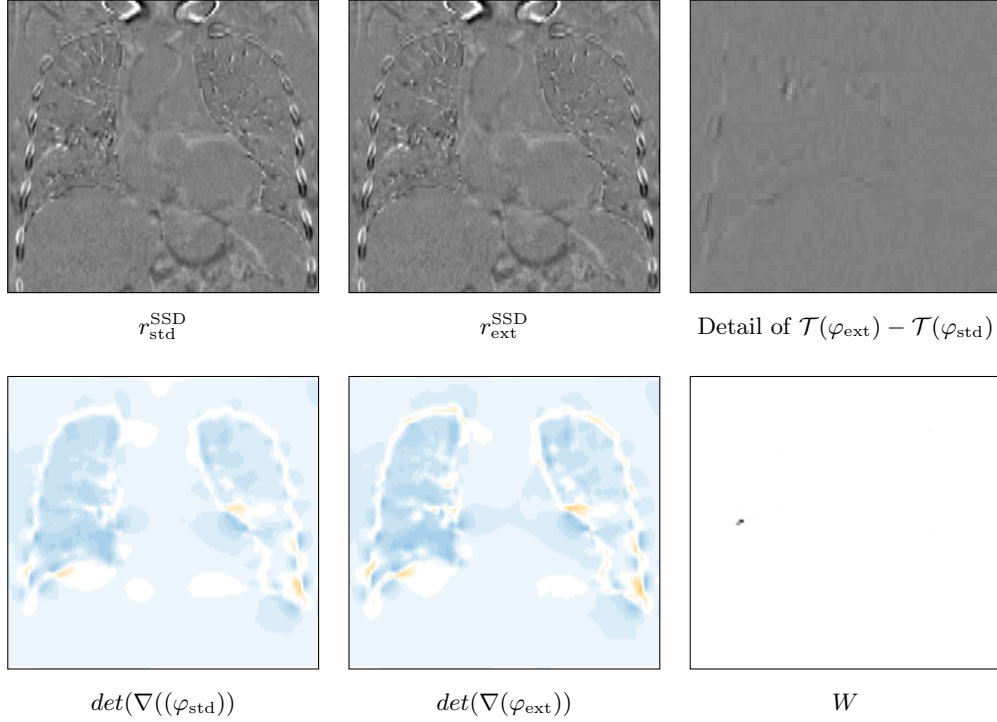


**Figure 4.2: (b)** Coronal view of the 3D results (using  $\mathcal{D}_W^{\text{SSD}}$ ) for case 5 of the CT lung database. The detail of the difference image of the warped templates  $\mathcal{T}(\varphi_{\text{ext}}) - \mathcal{T}(\varphi_{\text{std}})$  shows the diaphragm of the right lung. The unaltered lung images yield almost identical results for both approaches. The average TRE of this case can be found in Table 4.1.

of the contrast agent itself (in the  $\mathcal{T}$ , the contrast agent appears to have higher intensity values). In areas, where contrast agent in one image aligns with gas or tissue in the other image, big intensity differences and therefor high values for the distance measure arise. Here the difference between gas and contrast agent yields the biggest difference of intensities and thus the highest distance measure. This leads to strong deformations in the standard approach, for example in the inferior part of the intestines, close to the left pelvis, where the contrast agent is strongly compressed and moved towards the bone. This is shown in the introductory example Figure 1.1. Furthermore air from outside the patient is transformed to match gas in one part of the intestine, which even leads to a misalignment of

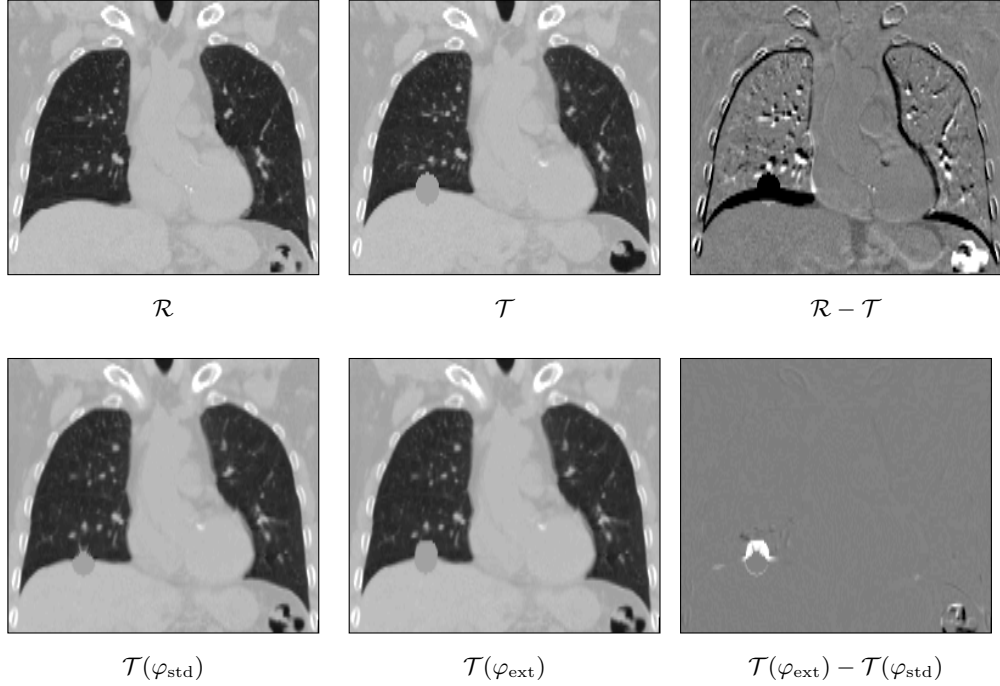


**Figure 4.3:** (a) Coronal view of the 3D results (using  $\mathcal{D}_W^{SSD}$ ) for case 3 of the CT lung database with a synthetic tumor located at the diaphragm of the right lung in the template image  $\mathcal{T}$ . A strong transformation of the tumor can be seen in the results of the standard approach. The relative volume change of the tumor in the transformed template images can be seen in Table 4.3 and the average TRE is listed in Table 4.2.

the spine, see  $\mathcal{T}$  in Figure 4.9. Those deformations are physically unrealistic and useless for practical applications. In the extended approach those critical regions which lead to unwanted deformations have a very low weight  $W$  in the distance measure and thus barely contribute. The transformed templates provided by the extended approach better represent anatomically reasonable images.

The third example (Figure 4.11 and 4.12) is an image pair which features contrast agent in parts of the intestines only in the template image  $\mathcal{T}$ . The transformed template of the standard approach  $\mathcal{T}(\varphi_{std})$  shows a compression of this contrasted region. Additionally the high intensity region is shifted to the location of the

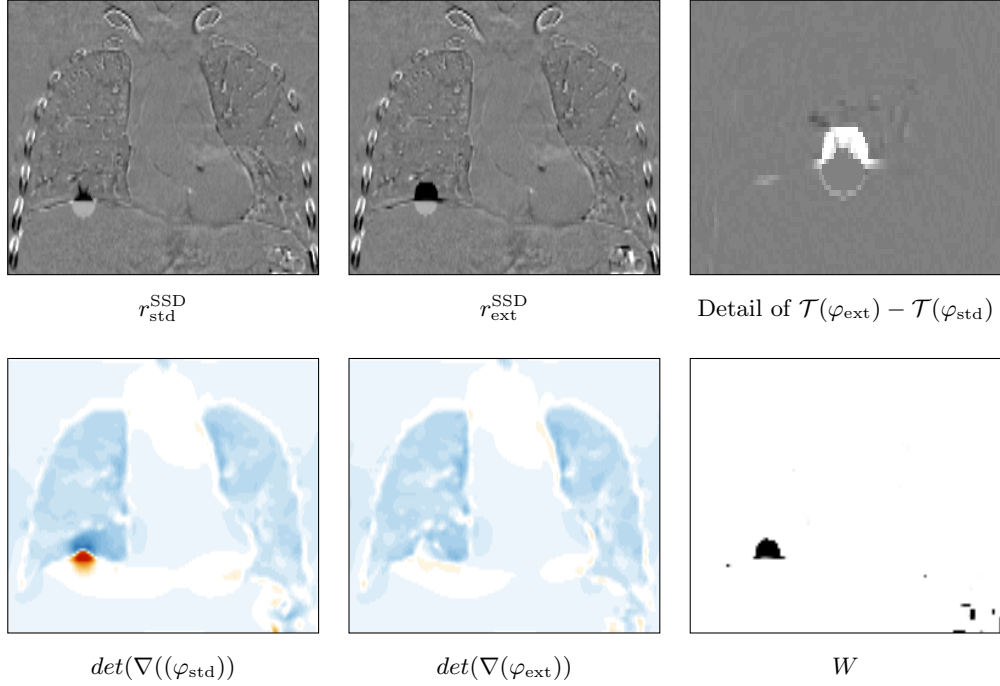


**Figure 4.4: (b)** Coronal view of the 3D results (using  $\mathcal{D}_W^{\text{SSD}}$ ) for case 3 of the CT lung database with a synthetic tumor located at the diaphragm of the right lung in the template image  $\mathcal{T}$ . The detail of the difference image of the warped templates  $\mathcal{T}(\varphi_{\text{ext}}) - \mathcal{T}(\varphi_{\text{std}})$  shows the tumor region. A strong transformation of the tumor can be seen in the results of the standard approach. The relative volume change of the tumor in the transformed template images can be seen in Table 4.3 and the average TRE is listed in Table 4.2.

liver in the reference image. Because the liver has higher intensity values than the surrounding tissue, the distance measure is decreased that way. Nonetheless the transformed template is unsuitable for certain clinical problems since the liver is badly aligned at the inferior edge. In the relevant figures the position of the inferior liver tip is indicated with red arrows. Accordant to the previous examples, the extended approach reduces the impact of the high distance measure at the contrast agent's location and provides a transformed template  $\mathcal{T}(\varphi_{\text{ext}})$  with a much better aligned liver.

## 4.4 NGF: CT Lung with Synthetic Tumor & CT-MRI Abdomen

The last experiments evaluate the effectivity of the proposed approach with the NGF distance measure. First the CT lung images with the synthetic tumor are evaluated in analogy to 4.1. This enables a direct comparison of the two used distance measure. Then multi-modal image data which cannot be registered reasonably with SSD, are evaluated with NGF as well. Both experiments show, that standard and extended approach yield basically the same results. The distinctive difference of the approaches with SSD demonstrated with the lung images cannot be seen for NGF because both approaches do not decrease the tumor volume.

The abdomen specific difficulties as described for the CT data also apply to the CT-MR data. Furthermore images of different modalities naturally feature different poses of the subject. Because tomographic imaging is sensitive to attenuation, larger amounts of radiation are needed to depict larger regions. Due to the potentially impairment of health caused by x-rays, radiologists try to minimize the radiation dose and thus the depicted anatomy. This causes that subjects are placed with their arms above the head. In contrast to CT scanners, MR scanners provide no ionizing radiation. For a more comfortable experience, subjects usually keep their arms along their body during MR scans with no cutback of the image quality. Especially for obese subjects this can lead to considerable changes of the body contour.

The multi-modal data used for this experiment consists of eight very heterogeneous image pairs. They consist of a reference CT scan and a template MR scan with various MR protocols used. Some were taken at the same day while some were taken up to 4 months apart. Most of the scans depict the abdomen with a differing field of view and some the whole body. Each image has a size of  $512 \times 512$  voxel in-slice and covering the abdomen or  $339 \times 34$  voxel in-slice for the combined whole body scan. The voxel size is between  $(0.66 \times 0.66)$  and  $(1.34 \times 1.34)$  mm<sup>2</sup> and slice thickness between 1 and 6 mm.

When conducting the experiments with NGF as the distance measure, the standard and the extended approaches show almost identical results. This can be seen in

the difference image of the transformed templates  $\mathcal{T}(\varphi_{ext}) - \mathcal{T}(\varphi_{std})$  in Figure 4.13 and 4.15. Although no improvement can be shown we can state, that the extended approach for NGF also does not impair the results compared with the standard approach.

Comparing the weights  $W$  of a lung case evaluated with SSD (Figure 4.4) and NGF (Figure 4.14) the fundamental differences caused by the choice of the similarity measure become clear. With the SSD approach only an area of the image corresponding to the tumor part inside of the lung and a few other smaller areas are black on the otherwise white depiction of the weight  $W$ . This demonstratively shows which areas receive a low weight (black) while the majority of the image receives a uniform high weight (white). On the other hand the weight of the NGF approach is mainly black. This is due to the different mode of operation of the distance measures. Low weights in  $W$  are caused by high values of the residual in the SSD setting. For NGF, low weights are caused by big angles between the image gradients or by zero gradients. The latter condition occurs relatively often, for example inside an organ like the liver. There only a few regions with distinct gradients can be found the rest almost equals zero. Big angles between the image gradients are more uncommon and as a result the low weights of  $P$  for NGF are in large part caused by zero gradients. Although these regions yield a high distance measure, they do not influence the deformation in a strong way, since (typical) transformations do not change the gradient essentially. A homogenous area will still be homogenous for the biggest part after a transformation, the gradient will stay zero and thus the distance measure will still be high. Since those areas are no big influence, the low weights introduced by  $W$  can barely influence the registration as well.

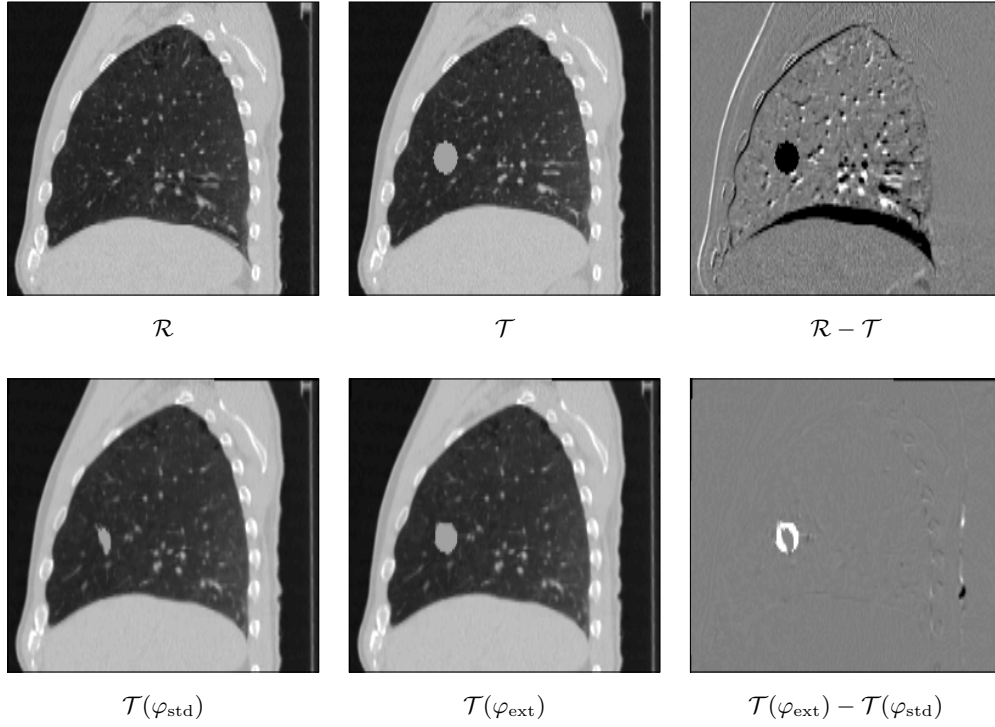


**Figure 4.5: (a)** Sagittal view of the 3D results (using  $\mathcal{D}_W^{\text{SSD}}$ ) for case 2 of the CT lung database with a synthetic tumor located at superior-dorsal edge of the right lung in the template image  $\mathcal{T}$ . A strong transformation of the tumor can be seen in the results of the standard approach. The relative volume change of the tumor in the transformed template images can be seen in Table 4.3 and the average TRE is listed in Table 4.2.

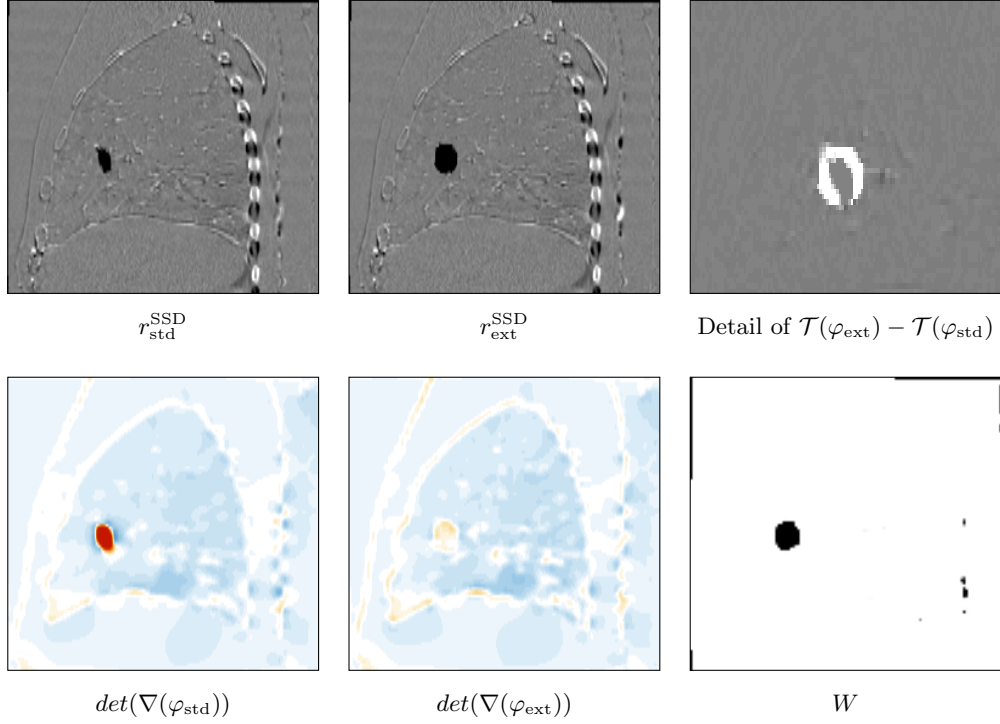


**Figure 4.6: (b)** Sagittal view of the 3D results (using  $\mathcal{D}_W^{\text{SSD}}$ ) for case 2 of the CT lung database with a synthetic tumor located at superior-dorsal edge of the right lung in the template image  $\mathcal{T}$ . The detail of the difference image of the warped templates  $\mathcal{T}(\varphi_{\text{ext}}) - \mathcal{T}(\varphi_{\text{std}})$  shows the tumor region. A strong transformation of the tumor can be seen in the results of the standard approach. The relative volume change of the tumor in the transformed template images can be seen in Table 4.3 and the average TRE is listed in Table 4.2.

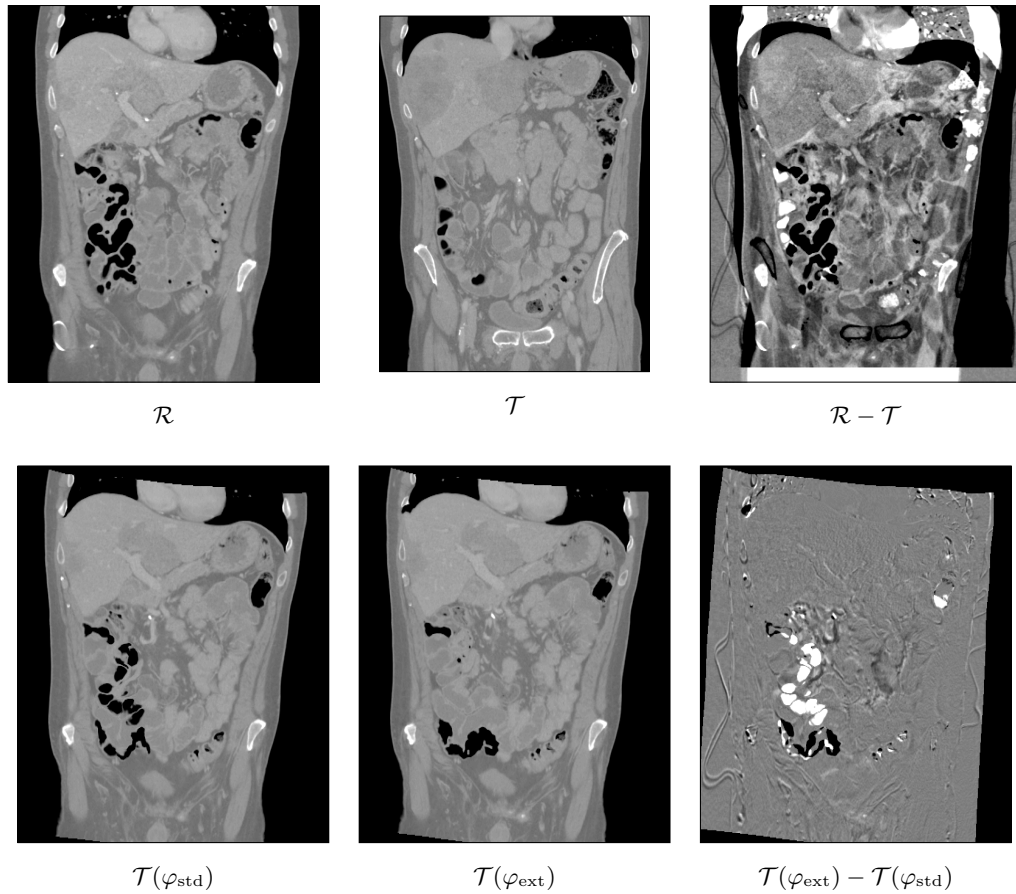


**Figure 4.7: (a)** Coronal view of the 3D results (using  $\mathcal{D}_W^{\text{SSD}}$ ) for case 2 of the CT abdomen database. This example demonstrates differences in the transformation of both approaches at the intestines.

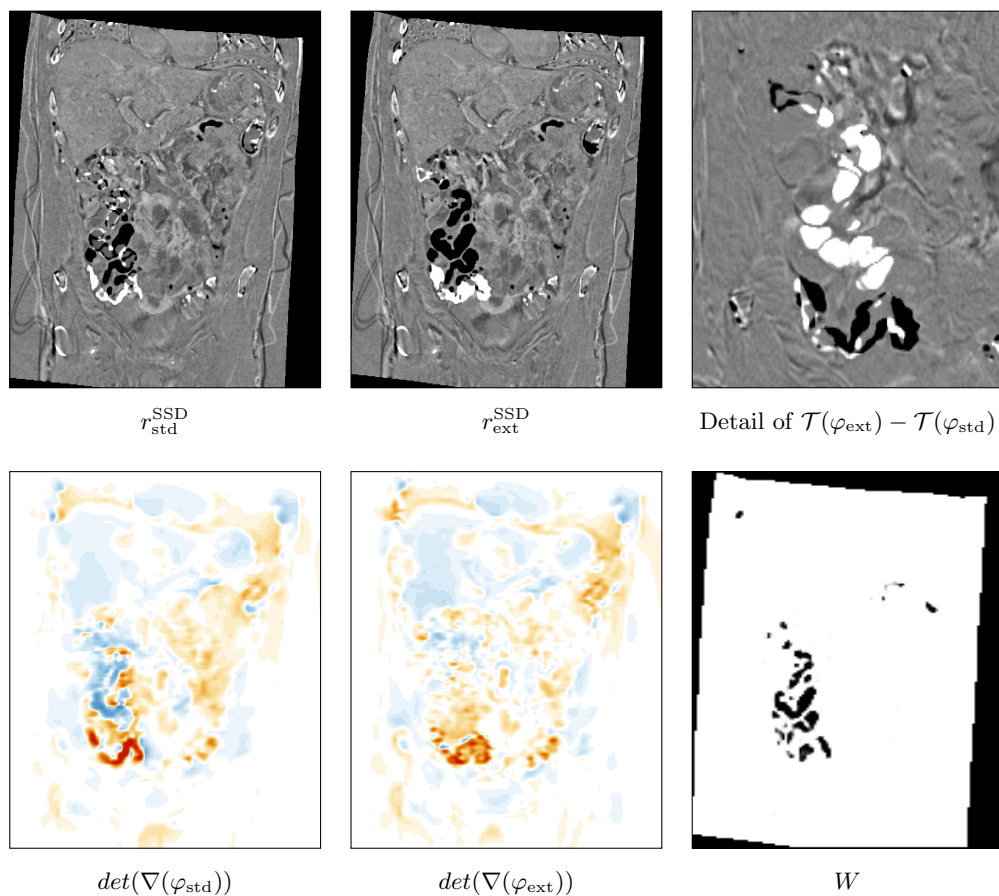


**Figure 4.8: (b)** Coronal view of the 3D results (using  $\mathcal{D}_W^{\text{SSD}}$ ) for case 2 of the CT abdomen database. The detail of the difference image of the warped templates  $\mathcal{T}(\varphi_{\text{ext}}) - \mathcal{T}(\varphi_{\text{std}})$  shows the contrasted intestines. This example demonstrates differences in the transformation of both approaches, with the standard approach stronger deforming the intestines.

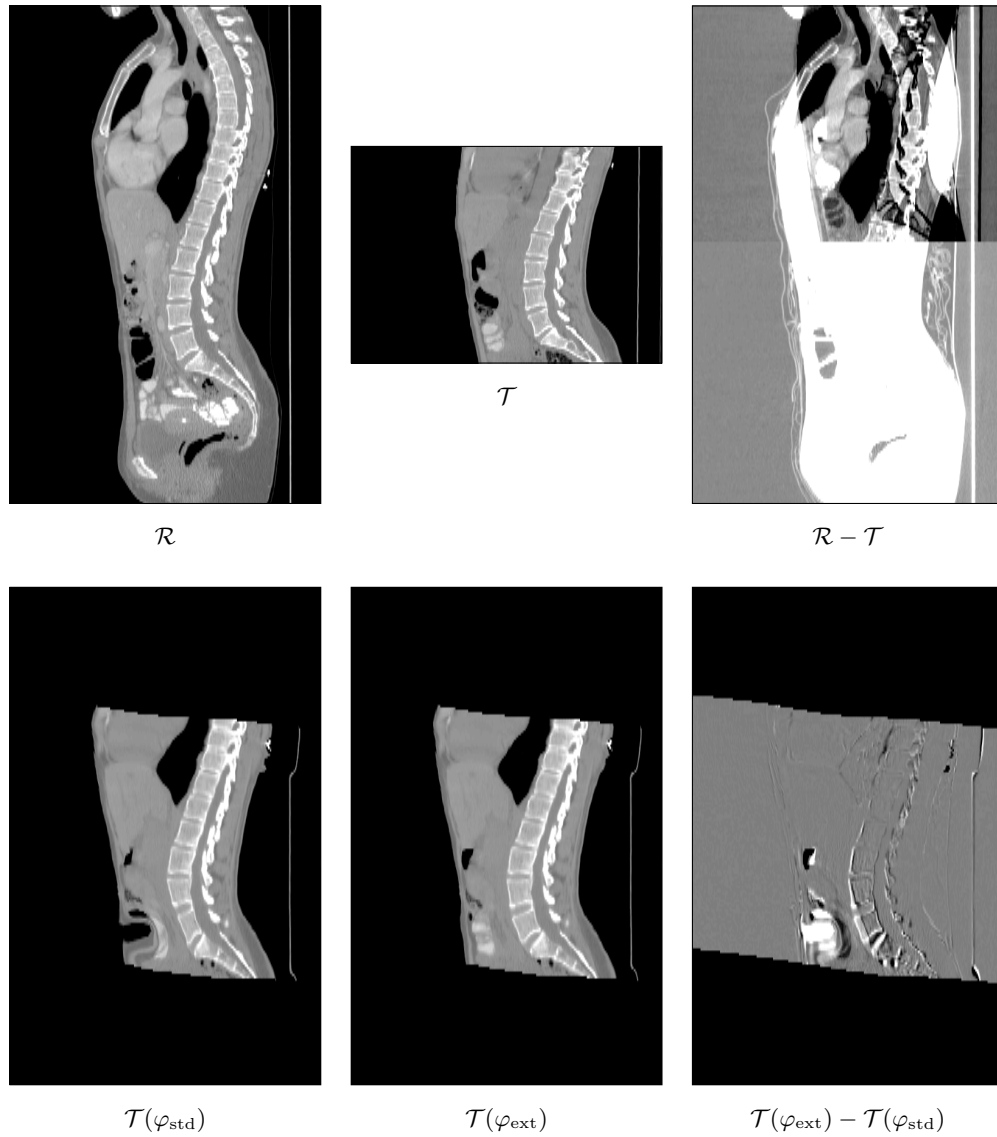


**Figure 4.9:** (a) Sagittal view of the 3D results (using  $\mathcal{D}_W^{\text{SSD}}$ ) for case 3 of the CT abdomen database. The standard approach transforms air into the abdomen and strongly deforms the surrounding anatomy while the extended approach yields an anatomical reasonable transformation.

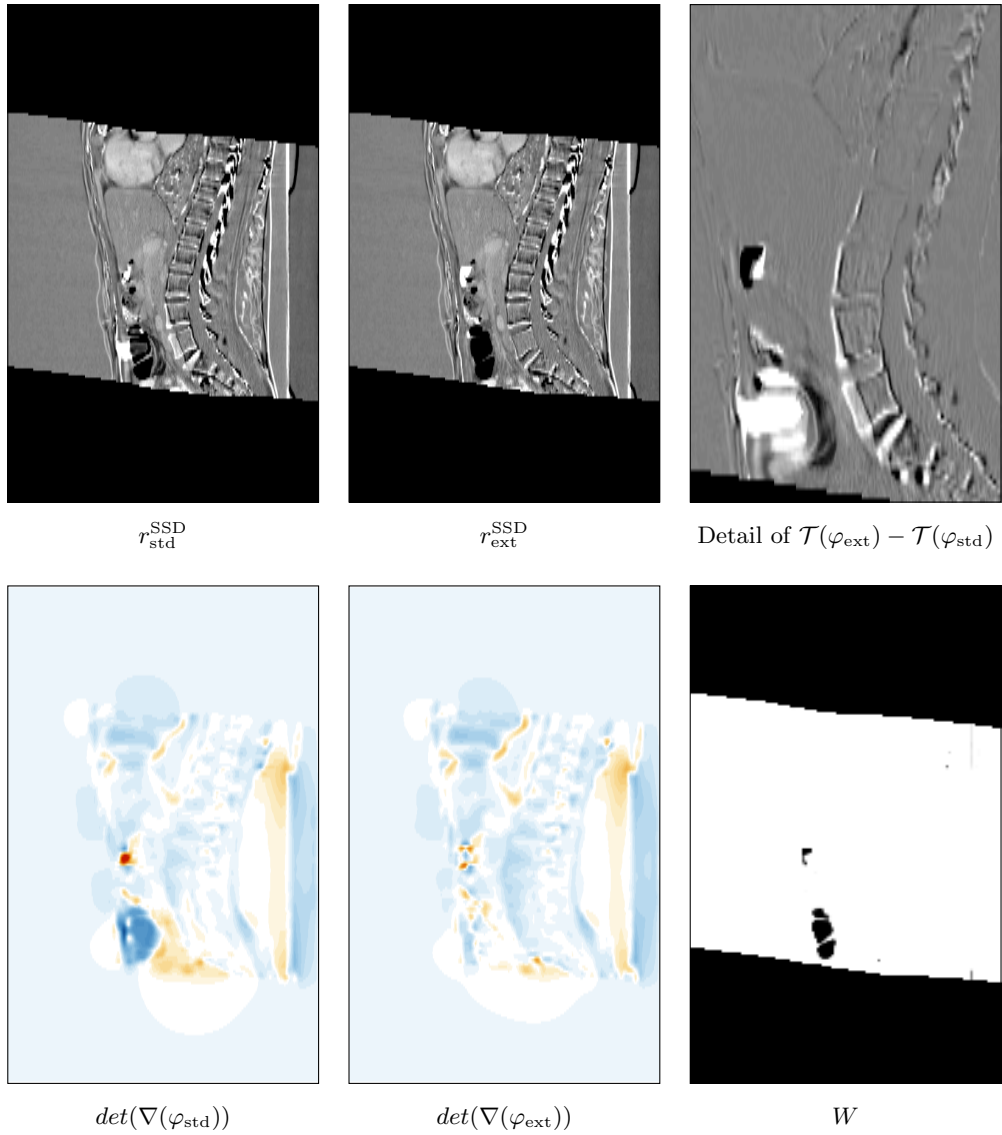


**Figure 4.10: (b)** Sagittal view of the 3D results (using  $\mathcal{D}_W^{\text{SSD}}$ ) for case 3 of the CT abdomen database. The detail of the difference image of the warped templates  $\mathcal{T}(\varphi_{\text{ext}}) - \mathcal{T}(\varphi_{\text{std}})$  shows the left inferior part of the intestines. The standard approach transforms air into the abdomen and strongly deforms the surrounding anatomy while the extended approach yields a anatomical reasonable transformation.

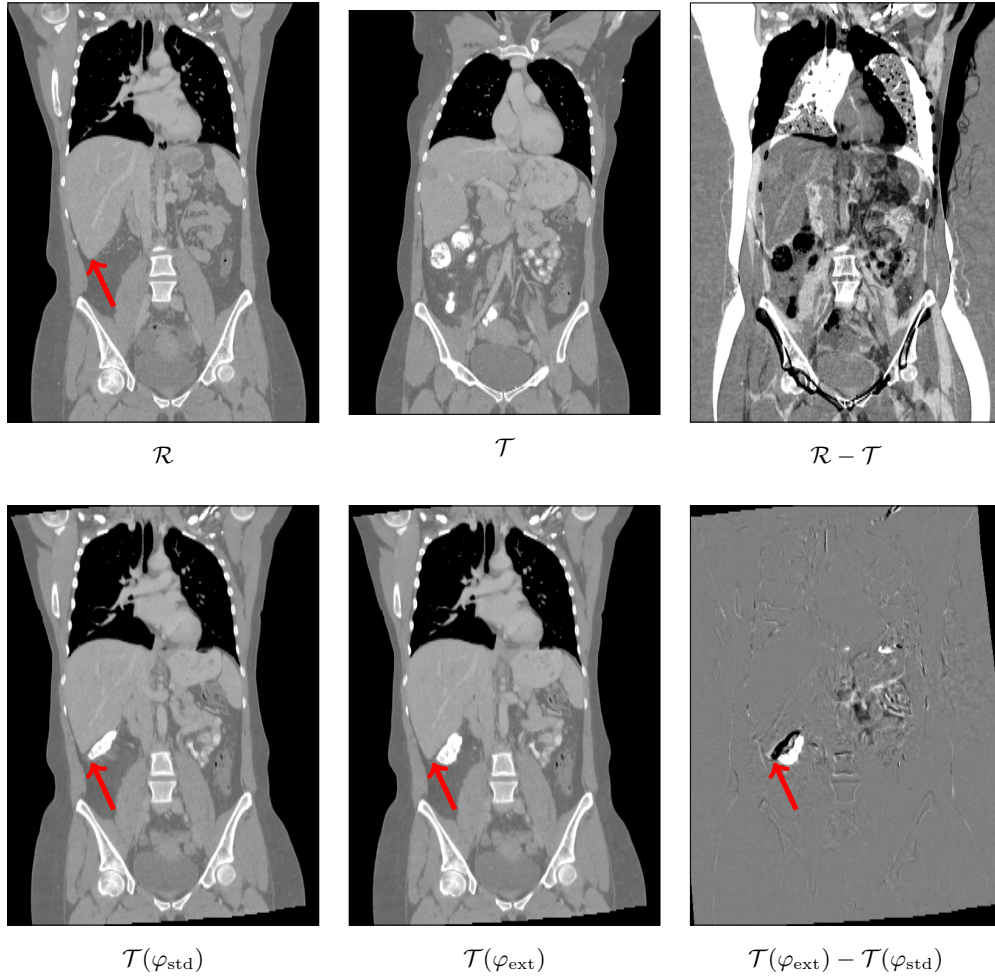


**Figure 4.11:** (a) Coronal view of the 3D results (using  $\mathcal{D}_W^{\text{SSD}}$ ) for case 9 of the CT abdomen database. A part of the intestines filled with contrast agent is transformed onto the liver by the standard approach. This impairs alignment of the liver. The Location of the inferior tip of the liver in the reference image is indicated by the red arrow in all relevant images, showing a better match by the extended approach.

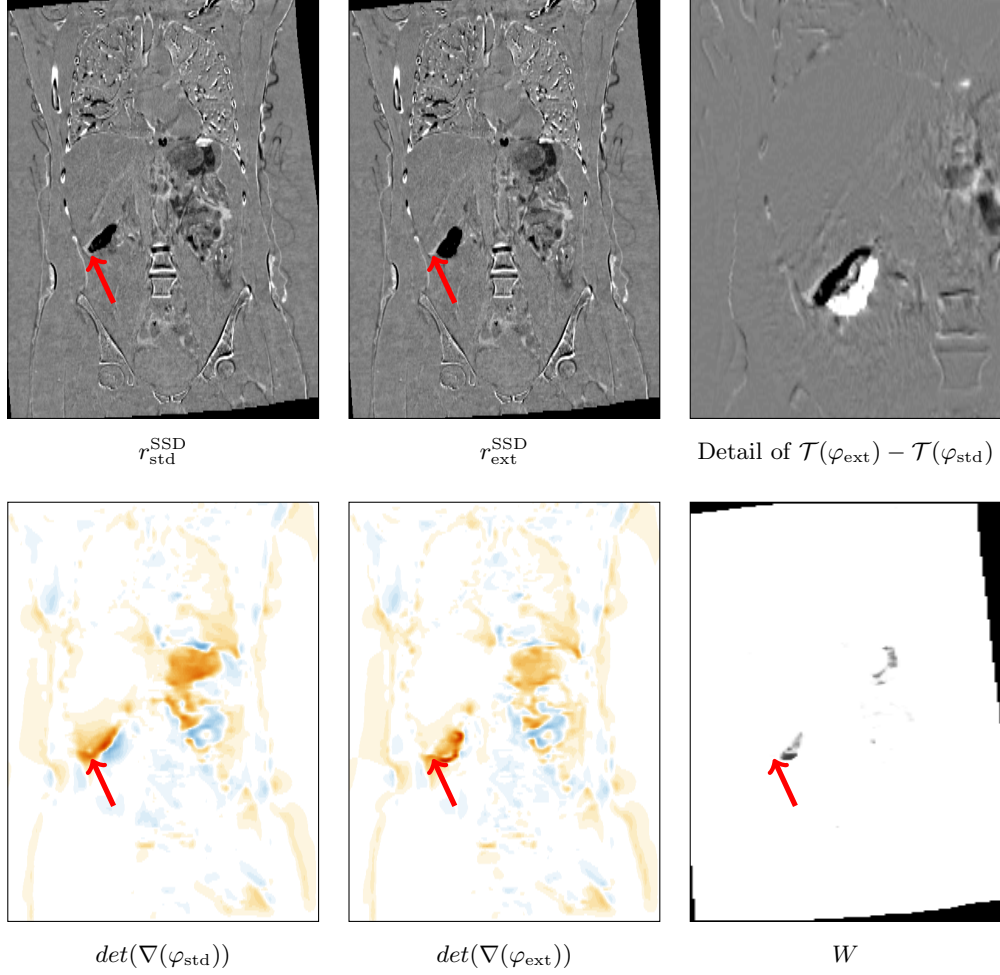


**Figure 4.12: (b)** Coronal view of the 3D results (using  $\mathcal{D}_W^{\text{SSD}}$ ) for case 9 of the CT abdomen database. The detail of the difference image of the warped templates  $\mathcal{T}(\varphi_{\text{ext}}) - \mathcal{T}(\varphi_{\text{std}})$  shows the liver. A part of the intestines filled with contrast agent is transformed onto the liver by the standard approach. This impairs alignment of the liver. The Location of the inferior tip of the liver in the reference image is indicated by the red arrow in all relevant images, showing a better match by the extended approach.

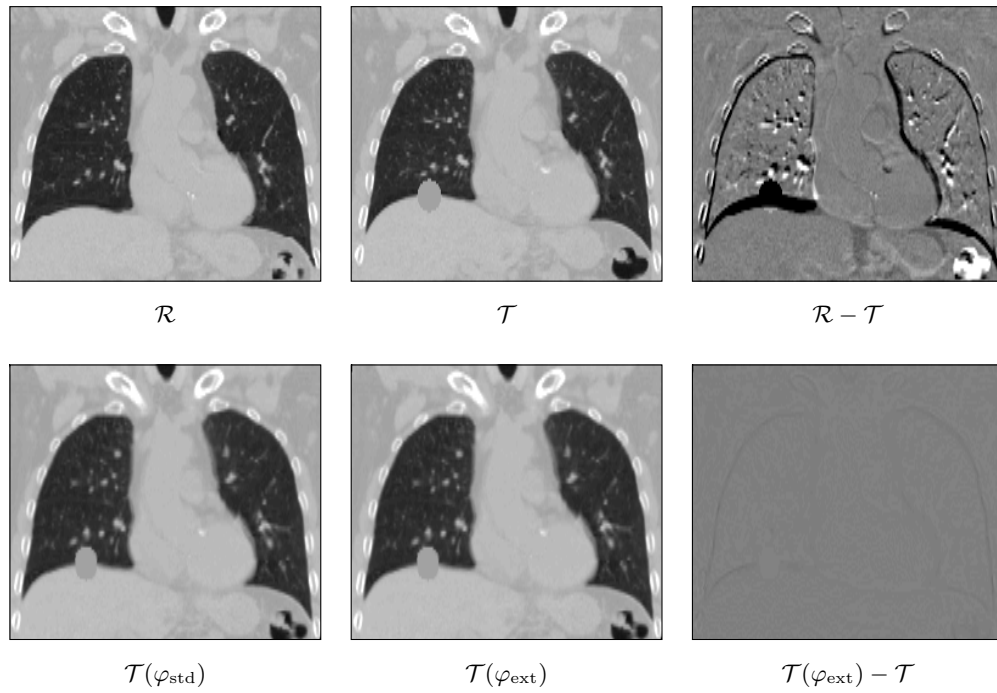


**Figure 4.13:** (a) Coronal view of the 3D results (using  $\mathcal{D}_W^{\text{NGF}}$ ) for case 3 of the CT lung database with a synthetic tumor located at the diaphragm of the right lung in the template image  $\mathcal{T}$ . Both approaches yield almost identical results.

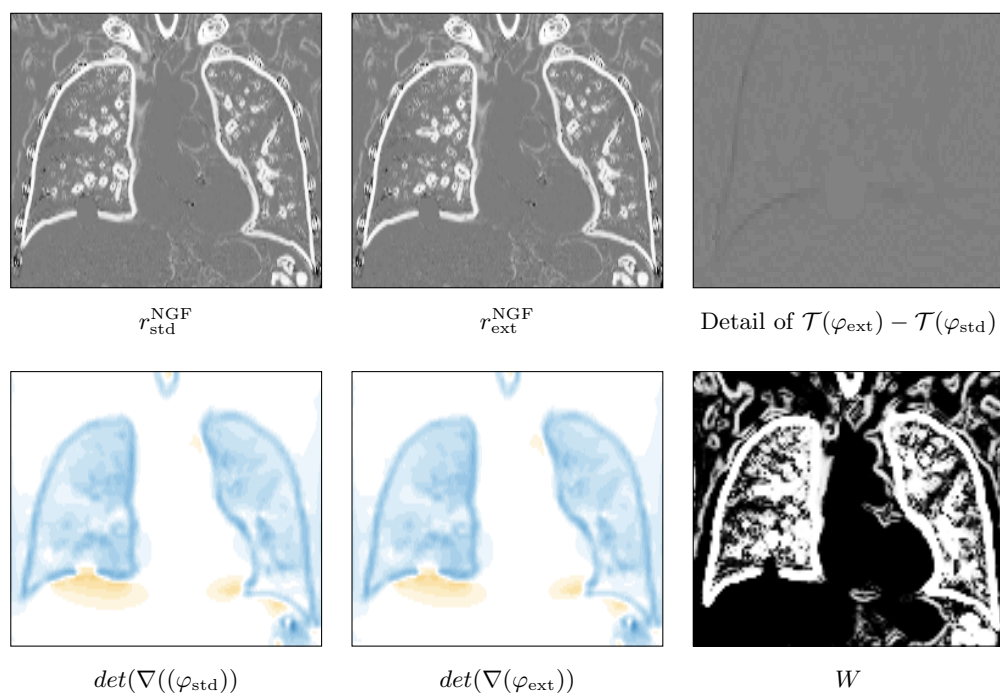


**Figure 4.14: (b)** Coronal view of the 3D results (using  $\mathcal{D}_W^{\text{NGF}}$ ) for case 3 of the CT lung database with a synthetic tumor located at the diaphragm of the right lung in the template image  $\mathcal{T}$ . The detail of the difference image of the warped templates  $\mathcal{T}(\varphi_{\text{ext}}) - \mathcal{T}(\varphi_{\text{std}})$  shows the tumor region. Both approaches yield almost identical results.

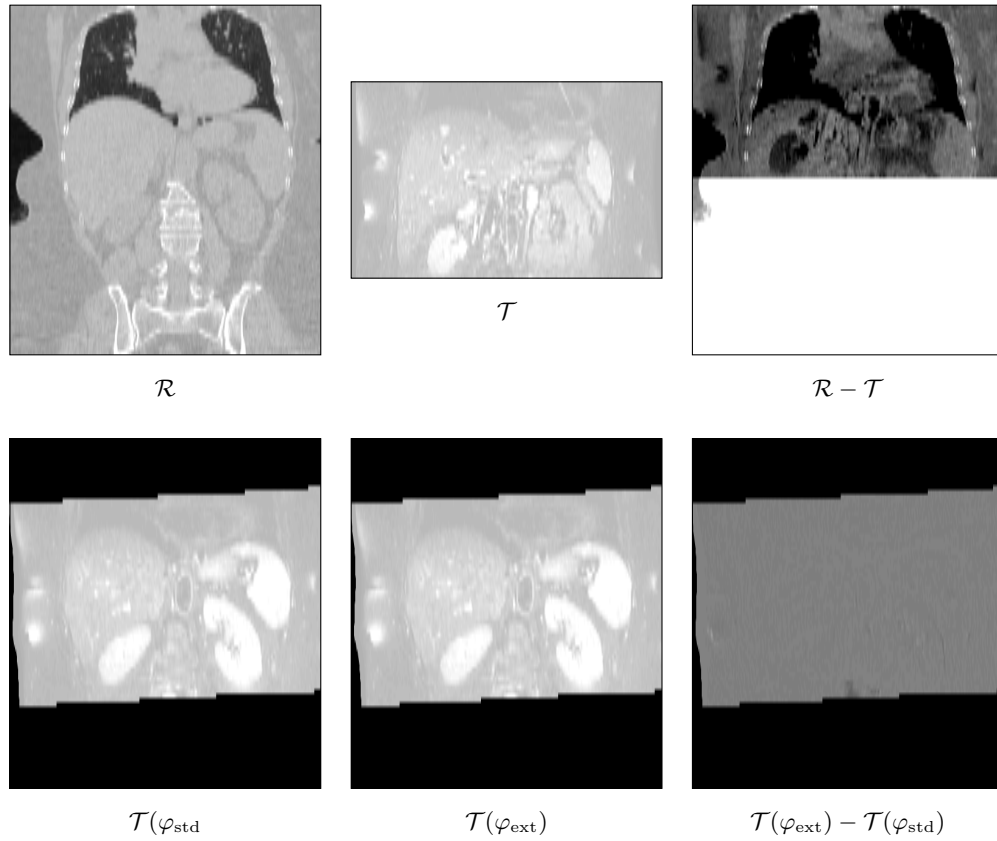


**Figure 4.15:** (a) Coronal view of the 3D results (using  $\mathcal{D}_W^{\text{NGF}}$ ) for case 1 of the CT-MRI abdomen database. Both approaches yield almost identical results.

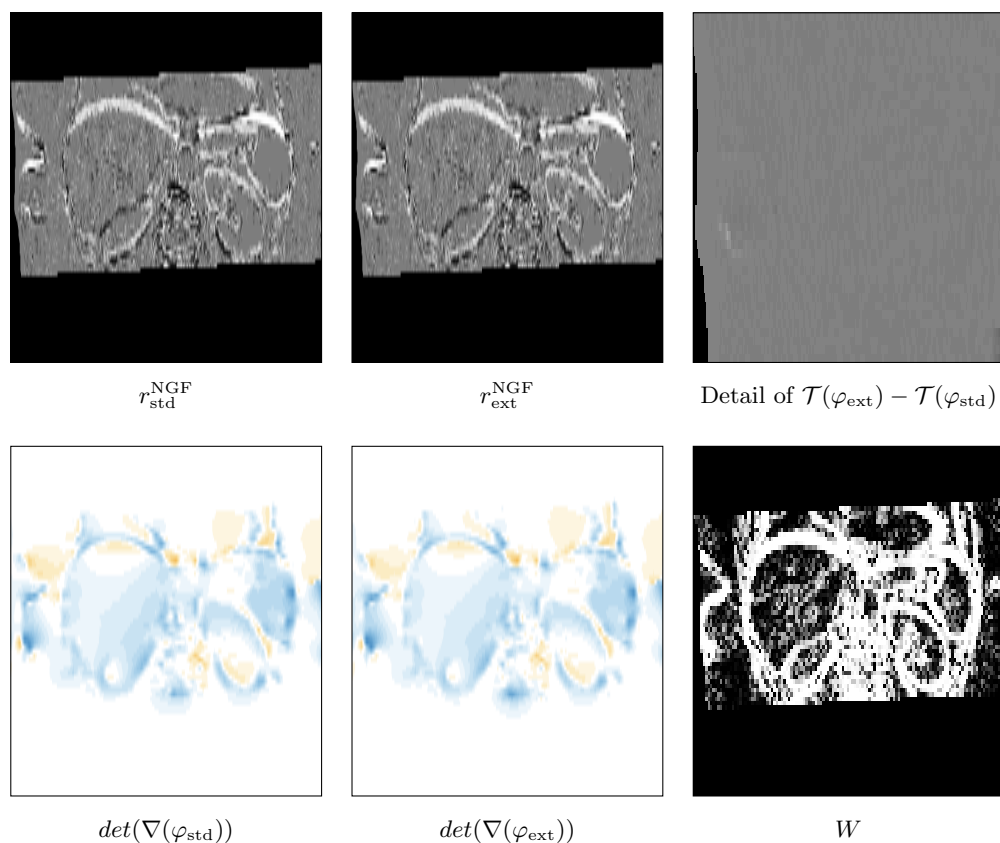


**Figure 4.16:** (b) Coronal view of the 3D results (using  $\mathcal{D}_W^{\text{NGF}}$ ) for case 1 of the CT-MRI abdomen database. The detail of the difference image of the warped templates  $\mathcal{T}(\varphi_{\text{ext}}) - \mathcal{T}(\varphi_{\text{std}})$  shows the liver. Both approaches yield almost identical results.



## 5 Conclusion and Outlook

In this thesis a standard variational registration algorithm is extended to handle non-corresponding regions. The weight  $W$  is automatically computed based on the Sum of Squared Differences (SSD) or the Normalized Gradient Field (NGF) distance measure, to reduce the effects of non-corresponding regions. The proposed approach is compared to a standard approach to demonstrate the superior handling of non-correspondences.

Experiments with lung CT images prove, that the extended approach with SSD yields transformations akin the standard approach when non-correspondences are not present. Evaluation of the average target registration error (TRE) shows only marginal higher accuracy of the standard approach. Non-corresponding regions are simulated by adding a synthetic tumor in one image of each lung image pairs. Evaluation of these experiments makes clear that the unwanted shrinking of the tumor by the standard approach is avoided in the proposed approach. We observe a significantly smaller average tumor shrinkage of 19% for central locations and 14% for peripheral locations compared to 66% and 43%, respectively, of the standard approach. For these cases the average TRE of both approaches is almost the same, indicating no relevant differences of the transformation in the rest of the lung. Real world data in the form of CT abdomen images featuring different kinds of non-correspondences support the findings of the previous experiments and yield different demonstrative examples for superior and physically more reasonable results. In the last experiment the altered lung CT data as well as multi-modal CT-MRI data were registered using the NGF distance measure. No significant differences of the approaches can be found for these cases.

While using the NGF distance measure could neither show improvement nor impairment of the results, the experiments with SSD document that regions without correspondences only slightly affect the registration when using the proposed approach.

---

In general the parameter choice strongly influences the registration. It can control the size of the low-weighted image regions and the grade of “binarization” of  $W$ , i.e. the steepness of the transition between minimum and maximum. With poor parameter choice the results of both approaches differ significantly with much worse results for the extended approach. Hence parameter choice is an important topic.

The two parameters used for the extended approach  $v$ ,  $p$  are chosen empirically. Optimization of the parameters for different scenarios could further improve the results. An automatic adaption depending on the image data could be investigated as well. It is also possible, that both parameters can be linked into a single parameter with comparable effects. First indications were found in some experiments but further analyses are necessary for any conclusion.

An interesting experiment would be to apply the proposed algorithm on the same data as different algorithms mentioned in the state of the art section 1.3. This could show the practical applicability of this approach and compare it to specialized methods. This brings up the choice between generalization and specialization. In the current form, our approach is kept as general as possible. Application specific knowledge could be included to optimize the results for a precise setting. An approach similar to the one described by Chitphakdithai et al. [14] is thinkable.

So far two distance measures were adapted for this approach. Theoretically other distance measure which provide a voxel-wise evaluation could be used as well. Future work may thus include exploration of other distance measures.

The examples presented in this thesis often feature a weight  $W$  which clearly locates the non-corresponding regions. Therefore a segmentation based on  $W$  could identify these regions for further processing. Different applications like tumor localization or contrast agent analysis are possible.

# Bibliography

- [1] Lisa Gottesfeld Brown. A survey of image registration techniques. *ACM Computing Surveys (CSUR)*, 24(4):325–376, 1992.
- [2] Jan Modersitzki. *FAIR: flexible algorithms for image registration*, volume 6. SIAM, 2009.
- [3] Jan Modersitzki. *Numerical Methods for Image Registration*. OUP Oxford, 2004.
- [4] Thorsten M. Buzug. *Einführung in die Computertomographie: mathematisch-physikalische Grundlagen der Bildrekonstruktion*. Springer, 2005.
- [5] André Collignon, Frederik Maes, Dominique Delaere, Dirk Vandermeulen, Paul Suetens, and Guy Marchal. Automated multi-modality image registration based on information theory. In *Information Processing in Medical Imaging*, volume 3, pages 263–274, 1995.
- [6] JP Lewis. Fast normalized cross-correlation. In *Vision Interface*, volume 10, pages 120–123, 1995.
- [7] Eldad Haber and Jan Modersitzki. Intensity gradient based registration and fusion of multi-modal images. In Rasmus Larsen, Mads Nielsen, and Jon Sporring, editors, *Medical Image Computing and Computer-Assisted Intervention-MICCAI 2006*, pages 726–733. Springer, 2006.
- [8] Björn Beuthin. *Restringierte medizinische Bildregistrierung*. PhD thesis, University of Lübeck, 2014.
- [9] Dongjin Kwon, Marc Niethammer, Hamed Akbari, Michel Bilello, Christos Davatzikos, and K Pohl. PORTR: Pre-operative and post-recurrence brain tumor registration. *Medical Imaging, IEEE Transactions on*, 33(3):651–667, 2014.

- [10] Sajendra Nithiananthan, Sebastian Schafer, Daniel J Mirota, J Webster Stayman, Wojciech Zbijewski, Douglas D Reh, Gary L Gallia, and Jeffrey H Siewerdsen. Extra-dimensional demons: a method for incorporating missing tissue in deformable image registration. *Medical Physics*, 39(9):5718–5731, 2012.
- [11] Nicha Chitphakdithai and James S Duncan. Non-rigid registration with missing correspondences in preoperative and postresection brain images. In T. Jiang, N. Navab, J.P.W. Pluim, and M.A Viergever, editors, *Medical Image Computing and Computer-Assisted Intervention–MICCAI 2010*, pages 367–374. Springer, 2010.
- [12] Nicha Chitphakdithai and James S Duncan. Pairwise registration of images with missing correspondences due to resection. In *Biomedical Imaging: From Nano to Macro, IEEE International Symposium on*, pages 1025–1028. IEEE, 2010.
- [13] Nicha Chitphakdithai, Veronica L Chiang, and James S Duncan. Non-rigid registration of longitudinal brain tumor treatment MRI. In *EMBC, Annual International Conference of the IEEE*, pages 4893–4896. IEEE, 2011.
- [14] Nicha Chitphakdithai, Kenneth P Vives, and James S Duncan. Registration of brain resection MRI with intensity and location priors. In *Biomedical Imaging: From Nano to Macro, IEEE International Symposium on*, pages 1520–1523. IEEE, 2011.
- [15] Floris F Berendsen, Alexis NTJ Kotte, Astrid AC de Leeuw, Max A Viergever, and Josien PW Pluim. Free-form registration involving disappearing structures: Application to brachytherapy MRI. In Hiroyuki Yoshida, Simon Warfield, and Michael W. Vannier, editors, *Abdominal Imaging. Computation and Clinical Applications*, pages 136–144. Springer, 2013.
- [16] Floris Berendsen, Alexis Kotte, Astrid de Leeuw, IM Jürgenliemk-Schulz, Max Viergever, and Josien Pluim. Registration of structurally dissimilar images in MRI-based brachytherapy. *Physics in Medicine and Biology*, 59(15):4033, 2014.
- [17] Senthil Periaswamy and Hany Farid. Medical image registration with partial data. *Medical Image Analysis*, 10(3):452–464, 2006.

- [18] Sven Kabus and Cristian Lorenz. Fast elastic image registration. *Medical Image Analysis for the Clinic: A Grand Challenge*, pages 81–89, 2010.
- [19] Jacques Hadamard. Sur les problèmes aux dérivées partielles et leur signification physique. *Princeton University Bulletin*, 13(49-52):28, 1902.
- [20] Chaim Broit. *Optimal registration of deformed images*. PhD thesis, University of Pennsylvania, 1981.
- [21] Uri M Ascher, Eldad Haber, and Hui Huang. On effective methods for implicit piecewise smooth surface recovery. *SISC*, 28(1):339–358, 2006.
- [22] Sven Kabus. *Multiple material variational image registration*. PhD thesis, University of Lübeck, 2007.
- [23] Magnus Rudolph Hestenes and Eduard Stiefel. Methods of conjugate gradients for solving linear systems. In *Journal of Research of the National Bureau of Standards*, volume 49, pages 409–436. National Bureau of Standards Washington, DC, 1952.
- [24] Eldad Haber and Jan Modersitzki. A multilevel method for image registration. *SIAM Journal on Scientific Computing*, 27(5):1594–1607, 2006.
- [25] Rick Durrett. *Probability: theory and examples*. Cambridge university press, 2010.
- [26] Jean-Pierre Florens. *Elements of Bayesian Statistics (Chapman & Hall/CRC Pure and Applied Mathematics)*. CRC Press, 1990.
- [27] Otto Forster. *Analysis 2*. Vieweg, 5 edition, 1999.
- [28] Richard Castillo, Edward Castillo, Rudy Guerra, Valen E Johnson, Travis McPhail, Amit K Garg, and Thomas Guerrero. A framework for evaluation of deformable image registration spatial accuracy using large landmark point sets. *Physics in Medicine and Biology*, 54(7):1849, 2009.
- [29] Sven Kabus, Tobias Klinder, Keelin Murphy, René Werner, and David Sarrut. *4D Modeling and Estimation of Respiratory Motion for Radiation Therapy*, chapter Validation and Comparison of Approaches to Respiratory Motion Estimation, pages 159–181. Springer, 2013.



# A Minimization of the Distance Measure

In this appendix details on the calculation of the derivatives summarized in Section 3.5 are given.

Starting point is the optimization of the functional  $\mathcal{J}$ . A stationary point of a Gâteaux-differentiable functional  $\mathcal{J}$

$$\mathcal{J}[\varphi] = \int_{\Omega} F[x, \varphi(x), \nabla\varphi(x)] dx \quad (\text{A.1})$$

is given by  $\varphi$ , if

$$\nabla_{\varphi} F(x) - \nabla \cdot \nabla_{\nabla_{\varphi}} F(x) = 0, \quad x \in \Omega. \quad (\text{A.2})$$

This can be found in [27] and it is derived in more detail for this setting in [22].

The result for the regularizer is given in 3.5 and only the calculation for the new extended distance measure will be shown here.

In this context  $\nabla_{\varphi}$  denotes the gradient operator with respect to the transformation  $\varphi$ . In the results this operator and the need for Gâteaux differentials vanishes because only the gradient with respect to the coordinates remains.  $(\nabla \cdot)_i$  denotes the  $i$ -th component of a derivative.

In the following let  $F$  denote the integrand of the distance measure  $\mathcal{D}$

$$F^{\text{SSD}} := [W^{\text{SSD}}(x) \cdot r^{\text{SSD}}(x)]^2 \quad (\text{A.3})$$

and

$$F^{\text{NGF}} := 1 - [W^{\text{NGF}}(x) \cdot r^{\text{NGF}}(x)]^2. \quad (\text{A.4})$$

Because  $\mathcal{D}$  does not depend on the gradient of  $\varphi$  the equation A.2 can be shortened to

$$\nabla_{\varphi} F(x) = 0, \quad x \in \Omega. \quad (\text{A.5})$$

The derivative of the transformed template  $\mathcal{T}_{\varphi}$  image is

$$(\nabla_{\varphi} \mathcal{T}_{\varphi})_i = \frac{\partial \mathcal{T}_{\varphi}}{\partial \varphi_i} = \frac{\partial \mathcal{T}_{\varphi}}{\partial x_1} \frac{dx_1}{d\varphi_i} + \frac{\partial \mathcal{T}_{\varphi}}{\partial x_2} \frac{dx_2}{d\varphi_i} + \frac{\partial \mathcal{T}_{\varphi}}{\partial x_3} \frac{dx_3}{d\varphi_i} \quad (\text{A.6})$$

$$= \frac{\partial \mathcal{T}_{\varphi}}{\partial x_i} = (\nabla \mathcal{T}_{\varphi})_i \quad (\text{A.7})$$

---

The second equality in (A.6) is due to the chain rule. By definition the transformation can be written as  $\varphi(x) = x + u(x)$ , where  $u$  denotes a vector field so that  $u(x)$  can be an arbitrary vector in  $\mathbb{R}^n$ . Therefore a local component of the transformation is  $\varphi_i(x) = x_i + u_i(x)$ . A derivation of  $x_k$  with respect to  $\varphi_i$  equals 0 for  $i \neq k$  and 1 for  $i = k$  because  $u_i$  is constant at  $x$ , which leads to (A.7).

## Calculation for SSD

Using the result of (A.7) the derivation of the residual is straightforward

$$\begin{aligned} (\nabla_{\varphi} r^{\text{SSD}})_i &= (\nabla_{\varphi} \mathcal{R})_i - (\nabla_{\varphi} \mathcal{T}_{\varphi})_i \\ &\stackrel{(A.7)}{=} -(\nabla \mathcal{T}_{\varphi})_i. \end{aligned} \quad (\text{A.8})$$

The derivatives of  $F^{\text{SSD}}$  can be calculated component wise as

$$\begin{aligned} (\nabla_{\varphi} F^{\text{SSD}})_i &= \left( \nabla_{\varphi} [W^{\text{SSD}} \cdot r^{\text{SSD}}]^2 \right)_i \\ &= 2 \cdot (W^{\text{SSD}} \cdot r^{\text{SSD}}) \cdot [(\nabla_{\varphi} W^{\text{SSD}})_i \cdot r^{\text{SSD}} + W^{\text{SSD}} \cdot (\nabla_{\varphi} r^{\text{SSD}})_i] \\ &\stackrel{(A.8)}{=} 2 \cdot (W^{\text{SSD}} \cdot r^{\text{SSD}}) \cdot [(\nabla_{\varphi} W^{\text{SSD}})_i \cdot r^{\text{SSD}} - W^{\text{SSD}} \cdot (\nabla \mathcal{T}_{\varphi})_i]. \end{aligned} \quad (\text{A.9})$$

The derivative of  $W$  is independent of the distance measure and can be computed with the quotient rule

$$\begin{aligned} (\nabla_{\varphi} W)_i &\stackrel{(3.11)}{=} s \cdot \frac{(\nabla_{\varphi} W_1)_i \cdot (W_1 + p) - W_1 \cdot (\nabla_{\varphi} W_1)_i}{(W_1 + p)^2} \\ &= s \cdot \frac{(\nabla_{\varphi} W_1)_i \cdot [(W_1 + p) - W_1]}{(W_1 + p)^2} \\ &= s \cdot \frac{(\nabla_{\varphi} W_1)_i \cdot p}{(W_1 + p)^2}. \end{aligned} \quad (\text{A.10})$$

The weights  $W_1$  have to be considered with respect to the distance measure. For the computation of the derivative of  $W_1^{\text{SSD}} = e^{-\frac{(r^{\text{SSD}})^2}{v \cdot \sigma^2}}$  the chain rule is applied

---


$$\begin{aligned}
(\nabla_{\varphi} W_1^{\text{SSD}})_i &= e^{-\frac{(r^{\text{SSD}})^2}{v \cdot \sigma^2}} \cdot \left( -\frac{(2r^{\text{SSD}} \cdot (\nabla_{\varphi} \mathcal{T}_{\varphi})_i) \cdot v \sigma^2 - (r^{\text{SSD}})^2 \cdot v \cdot (\nabla_{\varphi} \sigma^2)_i}{(v \cdot \sigma^2)^2} \right) \\
&\stackrel{(A.7)}{=} W_1^{\text{SSD}} \cdot \frac{(r^{\text{SSD}})^2 \cdot (\nabla_{\varphi} \sigma^2)_i - 2\sigma^2 \cdot r^{\text{SSD}} \cdot (\nabla_{\varphi} \mathcal{T}_{\varphi})_i}{v \cdot (\sigma^2)^2}. \tag{A.11}
\end{aligned}$$

Let  $\text{mean}(I(x))$  denote the mean of a discrete image  $I$  with a total of  $n$  voxels

$$\text{mean}(I(x)) = \frac{1}{n} \cdot \sum_{l=1}^n I(x_l)$$

The derivative of the variance of the residual

$$\begin{aligned}
(\nabla_{\varphi} \sigma^2)_i &= \frac{1}{n} \sum_{k=1}^n \left[ \left( \nabla_{\varphi} \left( (r^{\text{SSD}}(x_k)) - \text{mean}(r^{\text{SSD}}) \right)^2 \right)_i \right] \\
&= \frac{2}{n} \sum_{k=1}^n \left[ \left( \left( r^{\text{SSD}}(x_k) - \frac{1}{n} \cdot \sum_{l=1}^n (r^{\text{SSD}}(x_l)) \right) \right. \right. \\
&\quad \left. \left. \cdot \left( \nabla_{\varphi} \left( r^{\text{SSD}}(x_k) - \frac{1}{n} \cdot \sum_{l=1}^n (r^{\text{SSD}}(x_l)) \right) \right) \right)_i \right] \\
&\stackrel{(A.8)}{=} \frac{2}{n} \sum_{k=1}^n \left[ \left( (r^{\text{SSD}}(x_k)) - \text{mean}(r^{\text{SSD}}) \right) \cdot \left( -(\nabla_{\varphi} \mathcal{T}_{\varphi})_i(x_k) - \text{mean}((\nabla_{\varphi} \mathcal{T}_{\varphi})_i(x_k)) \right) \right] \\
&= -\frac{2}{n} \sum_{k=1}^n \left[ \left( (r^{\text{SSD}}(x_k)) - \text{mean}(r^{\text{SSD}}) \right) \cdot \left( (\nabla_{\varphi} \mathcal{T}_{\varphi})_i(x_k) - \text{mean}((\nabla_{\varphi} \mathcal{T}_{\varphi})_i(x_k)) \right) \right]. \tag{A.12}
\end{aligned}$$

---

## Calculation for NGF

Computation of the partial derivatives of  $F^{\text{NGF}}$  yields component-wise

$$\begin{aligned} (\nabla_{\varphi} F^{\text{NGF}})_i &= \left( \nabla_{\varphi} \left( 1 - [W \cdot r^{\text{NGF}}]^2 \right) \right)_i \\ &= -2 \cdot (W \cdot r^{\text{NGF}}) \cdot [(\nabla_{\varphi} F^{\text{NGF}})_i \cdot r^{\text{NGF}} + W \cdot (\nabla_{\varphi} r^{\text{NGF}})_i]. \end{aligned} \quad (\text{A.13})$$

The NGF distance measure has a more complex residual than SSD which makes the calculations a bit longish.

For the calculation of the derivative of the residual we substitute the scalar product by a sum and obtain

$$\begin{aligned} (\nabla_{\varphi} r^{\text{NGF}})_i &= \left( \nabla_{\varphi} \left\langle \frac{\nabla \mathcal{R}}{\|\nabla \mathcal{R}\|_{\varepsilon}}, \frac{\nabla \mathcal{T}_{\varphi}}{\|\nabla \mathcal{T}_{\varphi}\|_{\varepsilon}} \right\rangle \right)_i \\ &= \left( \nabla_{\varphi} \sum_{k=1}^d \frac{\frac{\partial \mathcal{R}}{\partial x_k}}{\|\nabla \mathcal{R}\|_{\varepsilon}} \cdot \frac{\frac{\partial \mathcal{T}_{\varphi}}{\partial x_k}}{\|\nabla \mathcal{T}_{\varphi}\|_{\varepsilon}} \right)_i \\ &= \sum_{k=1}^d \frac{\frac{\partial \mathcal{R}}{\partial x_k}}{\|\nabla \mathcal{R}\|_{\varepsilon}} \cdot \left( \nabla_{\varphi} \frac{\frac{\partial \mathcal{T}_{\varphi}}{\partial x_k}}{\|\nabla \mathcal{T}_{\varphi}\|_{\varepsilon}} \right)_i \\ &\stackrel{(\text{A.7})}{=} \sum_{k=1}^d \frac{\frac{\partial \mathcal{R}}{\partial x_k}}{\|\nabla \mathcal{R}\|_{\varepsilon}} \cdot \frac{\frac{\partial^2 \mathcal{T}_{\varphi}}{\partial x_i \partial x_k} \cdot \|\nabla \mathcal{T}_{\varphi}\|_{\varepsilon} - \frac{\partial \mathcal{T}_{\varphi}}{\partial x_k} \cdot \frac{\partial}{\partial \varphi_i} \|\nabla \mathcal{T}_{\varphi}\|_{\varepsilon}}{\|\nabla \mathcal{T}_{\varphi}\|_{\varepsilon}^2}. \end{aligned} \quad (\text{A.14})$$

In (A.14) the derivative of the norm of the template image needs to be calculated. The definition of the norm as  $\|\nabla I(x)\|_{\varepsilon} := \sqrt{\nabla I(x)^{\top} \nabla I(x) + \varepsilon^2}$  and multiple application of the chain rule yield

---


$$\begin{aligned}
(\nabla_\varphi \|\nabla \mathcal{T}_\varphi\|_\varepsilon)_i &= \left( \nabla_\varphi \left[ \varepsilon^2 \sum_{l=1}^d \left( \frac{\partial \mathcal{T}_\varphi}{\partial x_l} \right)^2 \right]^{\frac{1}{2}} \right)_i \\
&= \frac{1}{2} \left[ \varepsilon^2 \sum_{l=1}^d \left( \frac{\partial \mathcal{T}_\varphi}{\partial x_l} \right)^2 \right]^{-\frac{1}{2}} \cdot \left[ 2 \sum_{l=1}^d \frac{\partial \mathcal{T}_\varphi}{\partial x_l} \cdot \frac{\partial^2 \mathcal{T}_\varphi}{\partial \varphi_i \partial x_l} \right] \\
&\stackrel{(A.7)}{=} \frac{1}{\|\nabla \mathcal{T}_\varphi\|_\varepsilon} \cdot \sum_{l=1}^d \frac{\partial \mathcal{T}_\varphi}{\partial x_l} \cdot \frac{\partial^2 \mathcal{T}_\varphi}{\partial x_i \partial x_l}. \tag{A.15}
\end{aligned}$$

Combining equations A.14 and A.15  $\nabla_\varphi r^{\text{NGF}}$  can be brought into a more compact form. Therefor the fraction is split up and the definition of the residual is applied

$$\begin{aligned}
(\nabla_\varphi r^{\text{NGF}})_i &= \sum_{k=1}^d \frac{\frac{\partial \mathcal{R}}{\partial x_k}}{\|\nabla \mathcal{R}\|_\varepsilon} \cdot \frac{\frac{\partial^2 \mathcal{T}_\varphi}{\partial x_i \partial x_k} \cdot \|\nabla \mathcal{T}_\varphi\|_\varepsilon - \frac{1}{\|\nabla \mathcal{T}_\varphi\|_\varepsilon} \cdot \frac{\partial \mathcal{T}_\varphi}{\partial x_k} \cdot \sum_{l=1}^d \frac{\partial \mathcal{T}_\varphi}{\partial x_l} \cdot \frac{\partial^2 \mathcal{T}_\varphi}{\partial x_i \partial x_l}}{\|\nabla \mathcal{T}_\varphi\|_\varepsilon^2} \\
&= \sum_{k=1}^d \frac{\frac{\partial \mathcal{R}}{\partial x_k}}{\|\nabla \mathcal{R}\|_\varepsilon} \cdot \frac{\frac{\partial^2 \mathcal{T}_\varphi}{\partial x_i \partial x_k}}{\|\nabla \mathcal{T}_\varphi\|_\varepsilon} - \sum_{k=1}^d \frac{\frac{\partial \mathcal{R}}{\partial x_k}}{\|\nabla \mathcal{R}\|_\varepsilon} \cdot \frac{\frac{\partial \mathcal{T}_\varphi}{\partial x_k}}{\|\nabla \mathcal{T}_\varphi\|_\varepsilon} \cdot \frac{\sum_{l=1}^d \frac{\partial \mathcal{T}_\varphi}{\partial x_l} \cdot \frac{\partial^2 \mathcal{T}_\varphi}{\partial x_i \partial x_l}}{\|\nabla \mathcal{T}_\varphi\|_\varepsilon^2} \\
&\stackrel{(2.5)}{=} \sum_{k=1}^d \frac{\frac{\partial \mathcal{R}}{\partial x_k}}{\|\nabla \mathcal{R}\|_\varepsilon} \cdot \frac{\frac{\partial^2 \mathcal{T}_\varphi}{\partial x_i \partial x_k}}{\|\nabla \mathcal{T}_\varphi\|_\varepsilon} - \sum_{l=1}^d r^{\text{NGF}} \cdot \frac{\frac{\partial \mathcal{T}_\varphi}{\partial x_l} \cdot \frac{\partial^2 \mathcal{T}_\varphi}{\partial x_i \partial x_l}}{\|\nabla \mathcal{T}_\varphi\|_\varepsilon^2} \\
&= \sum_{k=1}^d \frac{\frac{\partial \mathcal{R}}{\partial x_k}}{\|\nabla \mathcal{R}\|_\varepsilon} \cdot \frac{\frac{\partial^2 \mathcal{T}_\varphi}{\partial x_i \partial x_k}}{\|\nabla \mathcal{T}_\varphi\|_\varepsilon} - r^{\text{NGF}} \cdot \frac{\frac{\partial \mathcal{T}_\varphi}{\partial x_k} \cdot \frac{\partial^2 \mathcal{T}_\varphi}{\partial x_i \partial x_k}}{\|\nabla \mathcal{T}_\varphi\|_\varepsilon^2} \\
&= \sum_{k=1}^d \frac{\frac{\partial^2 \mathcal{T}_\varphi}{\partial x_i \partial x_k}}{\|\nabla \mathcal{T}_\varphi\|_\varepsilon} \cdot \left( \frac{\frac{\partial \mathcal{R}}{\partial x_k}}{\|\nabla \mathcal{R}\|_\varepsilon} - r^{\text{NGF}} \cdot \frac{\frac{\partial \mathcal{T}_\varphi}{\partial x_k}}{\|\nabla \mathcal{T}_\varphi\|_\varepsilon} \right) \tag{A.16}
\end{aligned}$$

The derivative of  $W_1^{\text{NGF}}$  is calculated in analogy to the SSD case but with opposite sign:

$$(\nabla_\varphi W_1^{\text{NGF}})_i = -W_1^{\text{NGF}} \cdot \frac{(r^{\text{NGF}})^2 \cdot \nabla_\varphi \sigma^2 - 2\sigma^2 \cdot r^{\text{SSD}} \cdot (\nabla \mathcal{T}_\varphi)_i}{v \cdot (\sigma^2)^2}. \tag{A.17}$$



# Erklärung

Ich versichere an Eides statt, die vorliegende Arbeit selbstständig und nur unter Benutzung der angegebenen Hilfsmittel angefertigt zu haben.

Lübeck, 28. Februar 2015

David Drobny